Space Sci Rev (2013) 179:263–308
DOI 10.1007/s11214-013-9965-x

Radiation Belt Storm Probes Ion Composition Experiment (RBSPICE)

D.G. Mitchell · L.J. Lanzerotti · C.K. Kim · M. Stokes · G. Ho · S. Cooper · A. Ukhorskiy · J.W. Manweiler · S. Jaskulek · D.K. Haggerty · P. Brandt · M. Sitnov · K. Keika · J.R. Hayes · L.E. Brown · R.S. Gurnee · J.C. Hutcheson · K.S. Nelson · N. Paschalidis · E. Rossano · S. Kerem

Received: 30 June 2012 / Accepted: 1 February 2013 / Published online: 18 April 2013

Abstract The Radiation Belt Storm Probes Ion Composition Experiment (RBSPICE) on the two Van Allen Probes spacecraft is the magnetosphere ring current instrument that will provide data for answering the three over-arching questions for the Van Allen Probes Program: RBSPICE will determine "how space weather creates the storm-time ring current around Earth, how that ring current supplies and supports the creation of the radiation belt populations," and how the ring current is involved in radiation belt losses. RBSPICE is a time-of-flight versus total energy instrument that measures ions over the energy range from ∼20 keV to ∼1 MeV. RBSPICE will also measure electrons over the energy range ∼25 keV to ∼1 MeV in order to provide instrument background information in the radiation belts. A description of the instrument and its data products are provided in this chapter.

Keywords Magnetosphere · Ring current · Time-of-flight · Radiation belt · Space weather

1 Introduction

The idea, or concept, of a "ring current" around Earth and its association with geomagnetic storms began in the early days of the twentieth century. As Stern (1989) relates, Stoermer

D.G. Mitchell · C.K. Kim · M. Stokes · G. Ho · S. Cooper · A. Ukhorskiy · S. Jaskulek · D.K. Haggerty · P. Brandt · M. Sitnov · J.R. Hayes · L.E. Brown · R.S. Gurnee · J.C. Hutcheson · K.S. Nelson · N. Paschalidis · E. Rossano · S. Kerem
Space Department, The Johns Hopkins University Applied Physics Laboratory, Laurel, MD 20723, USA

L.J. Lanzerotti · K. Keika
Center for Solar Terrestrial Research, Department of Physics, New Jersey Institute of Technology, Newark, NJ 07102, USA

J.W. Manweiler (✉)
Fundamental Technologies LLC, Lawrence, KS 66046, USA
e-mail: Manweiler@ftecs.com

(1910, 1911, 1912) proposed this physical phenomenon as a way in which to handle a problem associated with his theory of charged particle motions in the geomagnetic field as related to actual observations. Somewhat later Adolf Schmidt (1924) proposed that such a ring current produced the "bays" (decreases in the ground-level geomagnetic field) measured in magnetogram traces during the main phase of a magnetic storm.

In their series of papers that provided a very early theory of the initiation and life of geomagnetic storms, Chapman and Ferraro (1931, 1932, 1933) postulated that a ring current at several Earth radii distance formed around Earth during the main phase of a storm. The ring current would be transient, being dissipated by interactions of the charged particles with the ambient atmosphere (Parker 1997). In this embodiment, the ring current somehow was the result of a neutral plasma cloud from the Sun that impacted Earth's magnetic field, first producing the short-lived "sudden commencement" enhancement of the ground-level field, and then the ring current. This ring current would be formed inside the Chapman-Ferraro geomagnetic cavity that was formed when the hypothesized plasma cloud encountered Earth's field. A major theoretical difficulty was how the particles from the cloud could penetrate the cavity (as discussed by Gillmor 1997, and by Stern 1989).

Hannes Alfvén published a nearly contemporaneous theory of magnetic storms (Alfvén 1939, 1940) wherein a ring current could be formed by the particles in a solar stream entering the geomagnetic field. These particles could access the field because they were convected by an electric field due to the motion of Alfvén's cloud that had a slight magnetic field embedded within (Stern 1989; Gillmor 1997). Alfvén was employing his "frozen-in" magnetic flux concept that had been largely overlooked by the research community. The disagreements between the Chapman and the Alfvén theories, which persisted for many years, are addressed by Akasofu (1970) and by Dessler (1970).

Prior to the discovery by Van Allen of Earth's radiation belts, S. Fred Singer (1957) had considered what the motions of charged particles would be if they somehow were to exist in the Earth's field, independent as to how they may have gotten there (since Stoermer's calculations of particle trajectories showed particles to be excluded from where a ring current might exist). Singer (1957) proposed that low energy charged particles could produce a ring current due to their longitudinal drift around Earth—"electrons one way, and protons the other—thus creating a completely stable ring current" (Singer 1957).

The particles discovered by Van Allen in his flights of Geiger-Mueller tubes on Explorers 1 and 3 (Ludwig 2011) were of too high an energy and too low in density to produce the hypothesized ring current. As the capabilities of instrumentation improved in the first decade of space flight, the energies of particles trapped in the geomagnetic field that could be measured decreased until particles with sufficient density in the range of the now-known ring current ($\sim$10 keV–$\sim$200 keV) could be detected during geomagnetic disturbances. The Explorer 26 satellite (December 1964–May 1967) flew a magnetometer and three instruments for measuring charged particles. One of these covered the proton energy range from 97 keV to $>$1700 keV and produced excellent data on ring current particles. Data obtained on April 18, 1965, during a magnetic storm demonstrated for the first time the importance of the ring current in the generation of a plasma instability (the drift mirror instability) in the magnetosphere and the acceleration of electrons at L $\sim$ 5 Re (Lanzerotti et al. 1969).

It is now well recognized that the plasma pressure of the inner magnetosphere is dominated by H, He, and O ions in the energy range from a few keV to order 400 keV (e.g., review by Kozyra and Liemohn 2003; Mitchell et al. 2003). Quite frequently the peak energy density is held by the charged particles with energies in the range of order 100 keV to order 200 keV. Ions are injected and energized in the inner magnetosphere during geomagnetic storms, building up hot plasma pressure that drives the electrodynamics of the magnetosphere-ionosphere system.

The hot plasma ring current has many effects, and many potential effects, on the magnetosphere and radiation belt populations as deduced from past measurements and theoretical work. In more recent years with more quantitative models of the geomagnetic field under normal and storm-time conditions (e.g., Sitnov et al. 2008), it has become apparent that the hot plasma can affect radiation belt particle motion in ways not conceived earlier. For example, the diamagnetic effect due to storm-time ring current can produce fast outward expansion of electron longitudinal drift orbits leading to their loss through the magnetopause. This effect can explain rapid depletion of electron fluxes over a broad region of the outer electron belt during storm main phase (e.g., Ukhorskiy et al. 2006; Turner et al. 2012). The hot plasma can produce "islands" in the drift paths of longitudinally-drifting ions (Ebihara and Ejiri 2000, 2003) and electrons (Ukhorskiy et al. 2006). The hot plasma also provides the energy source for multiple instabilities generating wave modes that drive local acceleration and loss (see review Thorne 2010) as well as radial transport of the outer belt electrons (e.g., Lanzerotti et al. 1969; Ukhorskiy et al. 2009).

One scenario, adapted by most of the existing ring-current models (e.g., Wolf et al. 1997; Kozyra et al. 1998; Liemohn et al. 1999; Jordanova et al. 2001; Fok et al. 2001; Ebihara and Ejiri 2003; Chen et al. 2007) is that the buildup of hot pressure is produced by steady-state magnetospheric convection. It is assumed in these models that the strong southward component of the interplanetary magnetic field (IMF), typical of a storm main phase, induces a large duskward electric field across the magnetotail. This cross-tail electric field drives earthward particle convection from the tail to the inner magnetosphere. In this framework the transport rates are directly controlled by the magnitude of the solar wind driver. The larger the southward IMF component, the stronger is the cross-tail electric field and the higher are the convection rates. It is expected that the convection electric field is larger during a storm main phase when the IMF is predominantly southward, and lower in a storm recovery phase when the IMF is mostly northward. This paradigm was questioned by recent statistical analysis of electric field data from the Geotail spacecraft (Hori et al. 2005); no substantial difference in the convection electric field was found between main and recovery phases.

It has also been suggested that the ring current buildup can be produced by the inductive electric field associated with dynamic reconfigurations of the magnetic field in the tail such as observed during magnetospheric substorms (e.g., Lui et al. 1987). Global images of ion injections into the ring current obtained with the use of neutral particle imaging techniques by the HENA instrument on the IMAGE spacecraft (e.g., Roelof et al. 1985; Henderson et al. 1997; Barabash et al. 1997; Mitchell et al. 2001, 2003; Brandt et al. 2002) show the highly dynamic nature of ion injections and the population changes during a geomagnetic storm.

In-situ ion measurements on spacecraft show that the transport and energization of ions in the magnetotail occurs largely in the form of discrete activations such as substorms and bursty bulk flows (Baumjohann et al. 1990; Angelopoulos et al. 1992; Shiokawa et al. 1997, 1998; Fairfield et al. 1998, 1999). Distinctive features of these impulsive events are high-speed plasma flow bursts with strong and steep increases of the tail magnetic field component (Bz) normal to the neutral plane. Such abrupt magnetic field changes, which make the stretched tail field more dipolar-like, are often referred to as dipolarization fronts (Nakamura et al. 2002; Runov et al. 2009).

Dipolarization fronts are routinely observed by the five THEMIS spacecraft in the magnetosphere tail ($X < -10R_E$) (e.g., Runov et al. 2009, 2011). It is not clear, however, whether these dipolarization events are related to the injections observed by IMAGE and whether injected particles can penetrate all the way into the ring current through the regions

Table 1 RBSPICE particle measurements

Level-1 Req.	Measurement	Cadence	Energy Range	Angle Res.	Energy Resolution
4.1.2.4	Medium energy protons	1 measure per minute	H: 10–10000 keV	15° × 12°	40 % at 0.3 MeV
4.1.2.5	Medium energy ions	1 measure per minute	He: 25–10000 keV, O: 40–10000 keV	15° × 12°	40 % at 0.05 MeV

of stronger dipolar magnetic fields of the inner magnetosphere—which may break the flows (e.g., Dubyagin et al. 2011). RBSPICE measurements on the two Van Allen Probes spacecraft will provide unique measurements necessary to differentiate between various mechanisms of the buildup of hot plasma pressure in the inner magnetosphere. The comparison of ions and field measurements at the two satellites will reveal whether the injections have a steady-state or a dynamic nature.

2 RBSPICE Hot Plasma Objectives and Measurement Technique

The three overarching science questions for the Van Allen Probes mission are

(a) Which physical processes produce radiation belt enhancement events?
(b) What are the dominant mechanisms for relativistic electron loss?
(c) How do ring current and other geomagnetic processes affect radiation belt behavior?

The RBSPICE instrument makes critical contributions to all of these science questions by determining how space weather creates the storm-time ring current around Earth and by determining how that ring current supplies and supports the creation of the radiation belt populations, and how it can also quickly reduce radiation belt particle intensities.

As discussed in the Introduction, for the last more-than-a-century, a ring current has been understood to be a critical part of the magnetosphere environment and magnetosphere dynamics. The generation of the hot plasma that comprises the ring current remains a major unknown in space plasma physics; therefore, the effects of this plasma environment on radiation belt particles are quite poorly understood. In order to obtain a comprehensive physical understanding of the radiation belts and their effects on technical systems that fly in them, it is mandatory that a comprehensive understanding of the physics of the hot magnetosphere plasmas be obtained by the Van Allen Probes Mission.

The basic particle measurements made by RBSPICE as required by the Van Allen Probes mission Level-1 science requirements are shown in Table 1.

The RBSPICE instrument is a time-of-flight (ToF) versus energy measurement system as shown schematically in Fig. 1.

The total energy of a particle that transits the detector system is measured with a solid state detector (SSD). Ion velocities are determined by measuring the flight time of a particle through the instrument (the particle's "time-of-flight"). The entry of a particle is recorded by detecting, in a microchannel plate (MCP), the secondary electrons that are emitted when the entering particle passes through the entrance aperture thin foil. The exit of the particle (prior to being measured in the SSD) is recorded by the transiting particle's passage through the exit foil with the detection in the MCP of the produced secondary electrons.

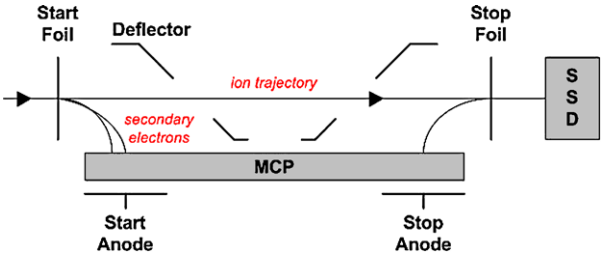

Fig. 1 Schematic illustration of RBSPICE measurement system

Table 2 RBSPICE performance requirements

Parameter	Required	Goal
Electron energies	None	25–1000 keV
Ion energies (measured, not necessarily discriminated)	H: 20–1000 keV, He: 30–1000 keV, O: 50–1000 keV	H: 10–10000 keV, He: 25–10000 keV, O/S: 40–10000 keV
Energy resolution	25 % for required energy range	20 % for required energy range. 50 % above and below required energy.
Time sampling	1/36 spin	1/36 spin
Angular resolution	15° × 12°	15° × 12°
Pitch Angle (PA) coverage	0–90° or 90°–180°	0–90° or 90°–180°
Time for full PA	1 Spin	1 Spin
Ion composition	H above 20 keV, He above 70 keV, O above 50 keV	H above 10 keV, He above 50 keV, O above 45 keV
Electron sensitivity, I = intensity (1 cm^2 sr), G = geometric factor × efficiency (cm^2 sr)	None	Sensor-G: 0,0036–0.00018, Pixel-G: 0.0007–0.000035, Up to 6 × 10^5/s counting
Ion sensitivity	$I = 1 \times 10^4$–1×10^8/cm^2 s sr	Sensor-G: 0.0036–0.00018, Pixel-G: 0.0007–0.000035, Up to 3.5 × 10^5/s count (TOP), Up to 6 × 10^5/s counting (E)

2.1 Science Requirements and Flow to Measurement Requirements

The Van Allen Probes Science Requirements Document provides for the inclusion of the RBSPICE instrument in the Van Allen Probes payload as the

> Radiation Belt Storm Probes Ion Composition Experiment (RBSPICE)—Determine how space weather creates what is called the "storm-time ring current" around Earth and determine how that ring current supplies and supports the creation of radiation populations.
>
> Overall RBSPICE performance requirements are listed in Table 2.

2.2 Relevant Program Level (Level 1) Requirements

Level 1 Requirements for the Van Allen Probes Mission are contained in Appendix C of the NASA *Living With a Star* (LWS) Program Plan.

2.3 RBSPICE-Relevant Mission Level Requirements (Level 2)

Level 2 requirements are maintained at the project level, and higher-level requirements flow from these:

Medium Energy Protons The Mission shall determine medium-energy proton distributions as follows:

- distribution energy range: 100 keV to 1 MeV
- distribution energy resolution (dE/E FWHM): at least 30 %
- distribution cadence: 1 distribution per 30 seconds
- distribution angular resolution: 20 degrees

Medium Energy Ion Composition (Protons) The Mission shall determine medium-energy ion composition (proton) distributions, as follows:

- distribution energy range: 20 keV to 300 keV
- distribution energy resolution (dE/E FWHM): 20 % at 20 keV, 30 % at 50 keV, 30 % at 300 keV
- distribution cadence: 1 distribution per 30 seconds
- distribution angular resolution: 30 degrees

Medium Energy Ion Composition (Helium) The Mission shall determine medium-energy ion composition (helium) distributions, as follows:

- distribution energy range: 20 keV to 300 keV
- distribution energy resolution (dE/E FWHM): 20 % at 20 keV, 30 % at 50 keV; 30 % at 300 keV
- distribution cadence: 1 distribution per 15 seconds
- distribution angular resolution: 30 degrees

Medium Energy Ion Composition (Oxygen) The Mission shall determine medium-energy ion composition (oxygen) distributions, as follows:

- distribution energy range: 40 keV to 300 keV
- distribution energy resolution (dE/E FWHM): 20 % at 40 keV, 20 % at 50 keV, 30 % at 300 keV
- distribution cadence: 1 distribution per 15 seconds
- distribution angular resolution: 30 degrees

2.4 RBSPICE Level 3–4 Performance Requirements

Level 3 and 4 Performance Requirements are maintained at the RBSPICE investigation level.

3 RBSPICE Mission Design Drivers

The Van Allen Probes Mission will intentionally be concentrated in the depths of the intense radiation environment of Earth's radiation belts. As such, the radiation environment imposes severe requirements on parts and system design.

The RBSPICE instrument addresses the intense natural charged particle environment by several techniques:

(a) The natural environment produces a dynamic range of foreground rates in the instrument. These are handled by the employment of very fast timing circuitry and two ranges of pixel size in the solid state detectors (SSD).
(b) The natural environment consists of very high rates of electrons, which produce a background that must be minimized. This is done by using very fast timing circuitry and the two ranges of pixel size in the SSDs. Background counts are measured in both the SSDs and the MCPs. There is an extra 4.5 g/cm^2 shielding around the SSDs. There is a "witness" SSD created by shielding a small pixel in one of the SSDs. Importantly, charged particle trajectory and stopping is modeled using the GEANT4 code and compared to instrument characterizations determined during calibrations.

The science requirements impose additional important mission design drivers:

(a) High temporal and angular resolution is required. This is achieved by fast electronics in binning the detector counts, by multiple view sectors, and by using the telemetry allocation as efficiently as possible.
(b) High energy resolution is required. This is achieved by selecting low noise detectors, by fast electronics for high time-of-flight timing resolution, and by efficiently using the telemetry allocation.

RBSPICE is designed and configured to overcome the challenges of the mission. Addressed here are: (1) visible light and UV; (2) huge dynamic range of input intensities expected for RBSPICE; (3) possibility of high fluxes of "out-of-band" low energy electrons and protons; (4) penetrating radiation.

3.1 Light, UV

The first defense against light and UV is collimation and mounting configuration, both designed to minimize the effects of sunlight. Direct entry of sunlight through the collimator would drive counting rates well above design limits on both the MCP and the SSDs. The second defense against both visible and UV light is filtering. The thin foils that serve to produce secondary electrons for timing pulses also serve to reduce the intensity of UV in the instrument, and the thicknesses of the foils are chosen to satisfy that requirement. In addition, visible light can overdrive the SSDs, raising their noise levels and leakage currents. Therefore the combination of foils and flashings on the detectors are the methods that reduce the light levels below those that result in such detector noise.

Background rejection on RBSPICE further relies, importantly, on valid event logic that requires coincidence among three separate detector signals: the TOF start, TOF stop, and SSD pulses must all fall within narrow timing windows for a valid event to be counted. Based on simulations of penetrating particles and UV, the expected maximum background rates R_{start}, R_{stop}, and R_{SSD} are all $\sim 10^4$ counts/s (the combined Front and Start foil thickness is selected to reduce UV sufficiently to meet this level). The predicted valid event rate is $R_{\mathrm{VE}} = R_{\mathrm{start}} \times R_{\mathrm{stop}} \times R_{\mathrm{SSD}} \times t_{\mathrm{TOF}} \times t_{\mathrm{SSD}}$, where $t_{\mathrm{TOF}} = 100$ ns and $t_{\mathrm{SSD}} < 1$ μs. This yields a false $R_{\mathrm{VE}} \sim 0.1$. Thus, for a typical (low) foreground rate of 1000 counts/s, the foreground/background (F/B) ratio is $\sim 10^4$. Even at a foreground rate of 1 c/s, the predicted F/B ratio caused by UV is 10.

3.2 Dynamic Range

RBSPICE is designed to handle a large dynamic range of ring current intensities, from levels below which the ring current pressure is unimportant to radiation belt dynamics up to the largest conceivable intensities in a super storm (well above any historical measurements).

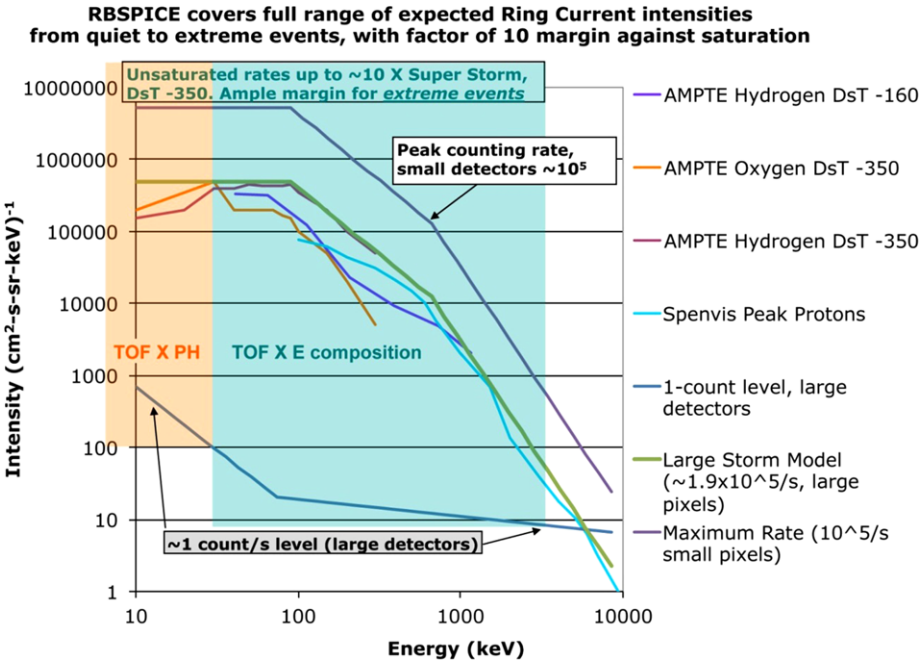

Fig. 2 RBSPICE coverage in intensity and energy

Figure 2 shows Earth ring current intensities and RBSPICE capabilities. Example ring current intensities obtained from measurements on the AMPTE satellite and from models are shown. The curves indicate the intensities corresponding to RBSPICE measurements of 1 count/s in an energy bin (minimum useful measurement), and 10^5 c/s over the full energy range using the small pixels of the SSDs (maximum calibrated intensity). For a "typical" Super Storm (Dst $= -350$ nT) RBSPICE would count at $\sim 1.9 \times 10^5$ in its large pixels (still in the calibrated range), or $\sim 10^4$ in its small pixels.

3.3 Low Energy Plasma

Using relatively thin ($\sim$10 micrograms/cm^2) foils to filter UV and produce secondary electrons for TOF determination, RBSPICE will allow protons as low as $\sim$3 keV to enter its TOF section. Therefore the TOF electronics must be capable of handling high rates generated by these particles, whose energy is below the primary energy range requirements and goals for calibrated characterization of the environment. Likewise, plasma electrons can penetrate the thin foils and either produce secondary electrons or directly strike the MCP, producing counts. Figure 3 provides the efficiencies for secondary electron generation in the Start foil, as a function of electron energy.

To reduce the susceptibility of RBSPICE to plasma electrons, as well as low energy protons, particles entering the instrument encounter two separate, independent foils whose total thickness is driven by the requirements for UV absorption. The first of these two foils is mounted on one of the perforated cylindrical sections (blades) that make up the RBSPICE collimator. Encountering this foil, transmitted low energy particles are typically scattered by large angles into trajectories that are stopped by subsequent collimator blades, and never

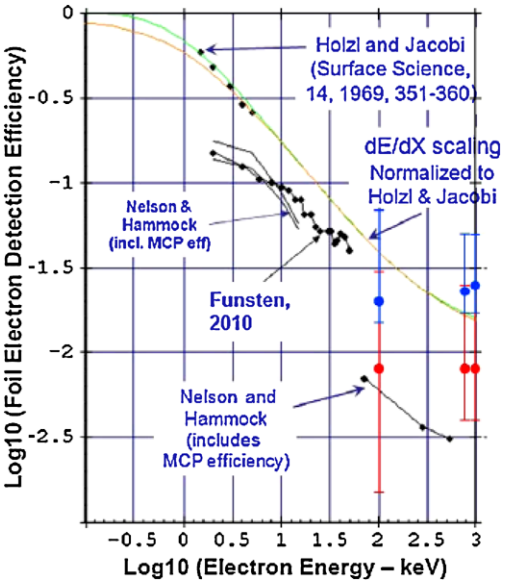

Fig. 3 Efficiency of secondary electron generation from energetic electrons passing through thin carbon foils as a function of primary electron energy

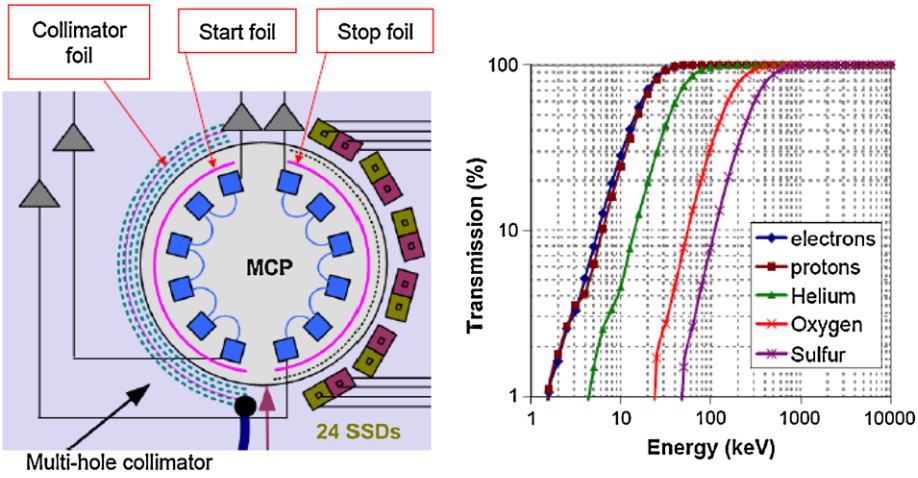

Fig. 4 *Left*: configuration of sensor head; *Right*: transmission efficiency as a function of energy of particle species

strike the second (start) foil. The start foil covers the entrance to the TOF section, but only a small fraction of the original low energy ion and electron intensities reach it, thus limiting background rates.

In the absence of a magnet to sweep out low energy contaminating electrons, the collimator foil suppresses (by scattering into the collimator) the lowest energy electrons (and protons), thereby preventing "start" saturation by the most intense low-energy plasma particles.

The right hand side of Fig. 4 shows the drop off in efficiency to low energy particles that result from scattering in the front foil and the subsequent loss in the collimator. The

figure also includes the effects of scattering in the start foil causing incident particles to miss striking the stop foil and registering a TOF signal. Less than 6 % of the incident protons and electrons are transmitted for particle energies below ∼10 keV.

3.4 Penetrating Radiation

At the high energy end of the spectrum, RBSPICE is designed to minimize the effects of penetrating radiation. RBSPICE includes a minimum of ∼3.8 g/cm^2 WCu shielding, capable of stopping electrons up to about 5 MeV, and protons up to about 40 MeV. This is sufficient to greatly reduce detector rates driven by penetrating particles in all but the heart of the inner radiation belt (where RBSPICE has no measurement requirements). In the outer electron belt, penetrating electrons above 5 MeV will at times produce elevated rates on the individual detectors, but the intensities are not sufficient to drive the rates high enough to produce significant numbers of false valid events (start-stop pairs or TOFs, and TOFs with correlated SSD energy pulses).

Energetic electrons entering through the collimator, for which RBSPICE has no mission requirements, nevertheless will drive high rates in the SSDs (the MCPs have relatively low efficiency response to the electrons). Calculations using a worst case electron spectrum as the input (the so-called Baker-Mitchell-O'Brien spectrum after those who compiled historical data to construct the spectrum) show that under extreme circumstances, the RBSPICE ion system will see rates close to, but not exceeding, the instrument's design maximum. Under these conditions, the false valid event rates will be elevated, but not sufficiently to obscure or distort the measurement of ring current intensities at meaningful (significant distortion of the main geomagnetic field) levels.

RBSPICE also includes a "witness" electron detector. This detector is at one extreme end of the SSD semi-circle and is covered with a copper/tungsten (CuW) shield. This detector sits at an angle already physically blocked by one end of the collimator, which is filled (no holes) in that look direction to avoid entry of sunlight into RBSPICE in flight. This detector serves as a monitor of penetrating background radiation (radiation belt ions and electrons, and cosmic rays).

3.5 RBSPICE Viewing

The Van Allen Probes spacecraft spins about its Z axis, sweeping the RBSPICE fan-shaped field of view through 360° every ∼12 second spin. RBSPICE is mounted at an angle to the spacecraft such that its anti-sunward look direction is approximately centered on the spin axis (see Sect. 4.4). This mounting arrangement provides one angular direction that is unmodulated by the spin, allowing for unaliased detection of changes in the particle environment. The tilt also prevents direct sunlight from entering the RBSPICE Field of View (FOV). The RBSPICE collimator FOV is blocked through an additional 12 degrees from its sunward edge to eliminate off-radial sunlight paths. This blockage also blinds one of the RBSPICE electron SSDs; that SSD is also covered with a copper-tungsten (CuW) shield so that it can serve as a background monitor (Sect. 3.4).

4 RBSPICE Instrument

4.1 Principle of Operation

RBSPICE, shown in Fig. 5, measures ion energy, direction, and composition using Time-of-Flight by Energy (TOF × E) and Time-of-Flight by Pulse Height (TOF × PH) techniques

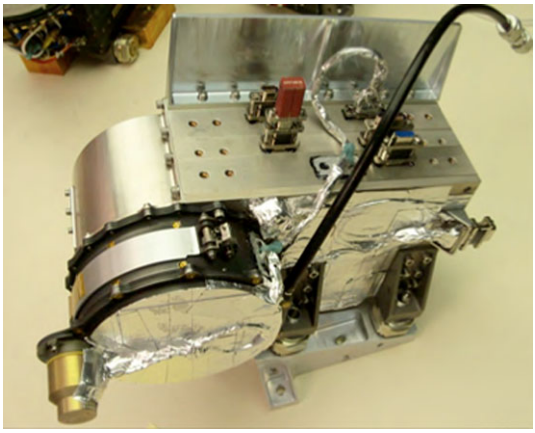

Fig. 5 RBSPICE instrument on spacecraft bracket prior to spacecraft integration

(see Fig. 1). The RBSPICE sensor head contains a Micro Channel Plate (MCP) detector that measures particle TOF and six solid state detectors (SSD) that measure particle energy. Secondary electrons that are generated by ions passing through the entry and exit foils are detected by the timing anodes and their associated pre-amplifiers to measure the ion TOFs. Event energy and TOF measurements are combined to derive ion mass and to identify particle species.

4.1.1 Ion Sensors

Prior to an ion passing through the TOF head, the ion first passes through a thin foil in the collimator. The ion will emerge as an ion or a neutral. If it emerges as an ion, it is accelerated by a negative 2.6 kV potential on the TOF start foil; after passing through the stop foil the ion can have a changed charge state. If the particle remains an ion after the stop foil, the ion is decelerated by 2.5 kV prior to reaching a SSD. (Below about 30 keV a proton has less than a 50 % chance of remaining charged upon exiting either foil. At 10 keV, the probability for remaining charged drops to about 20 %.) Secondary electrons from the foils are electrostatically guided onto the MCP, providing the start and stop signals for the TOF measurements.

The segmented MCP anodes, with two start and two stop anodes for each of the six angular segments determine the direction of travel, a parameter that is required for lower energy ions that do not yield a SSD signal above the detector threshold. A 500-volt accelerating potential between the foil and the MCP surface controls the electrostatic steering of secondary electrons. The dispersion in electron transit time is less than 1 nsec.

Ion energy measurements using the ion detectors are combined with coincident TOF measurements to derive particle mass and identify particle species. Particles are measured from less than 10 keV to above 1 MeV; they are discriminated in the energy system above about 25 keV for protons and above about 80 keV (total energy) for heavy ions (such as the CNO group). Lower-energy ion fluxes are measured using TOF-only measurements; detection of MCP pulse height provides a coarse indication of low-energy particle mass. The sensitivity to higher energy ions (those with energies above the SSD channel thresholds) can be adjusted by selecting large or small SSD pixels.

The RBSPICE acceptance angle is fan-like, and measures 160° by 12° with six 26.7° look directions. The total ion geometric factor for RBSPICE is greater than 0.0003 cm^2-steradian (the large SSD pixels). Particle direction is determined by the particular SSD pixel

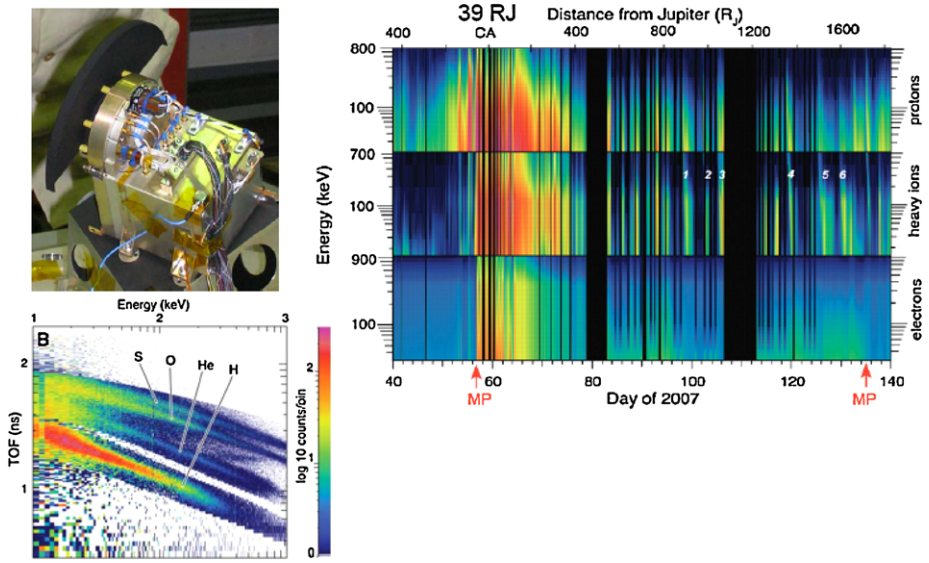

Fig. 6 New Horizons PEPSSI Instrument Heritage

in which it is detected as well as the locations of the TOF start and stop pulses. This direction information is used together with magnetic field data from the EMFISIS instrument to determine the particle pitch angles in the data processing by the RBSPICE Science Operations Center (SOC); see Sect. 7.

4.1.2 Electron Sensors

Although not a science requirement for RBSPICE, the instrument also has the capability (based on heritage designs) to measure electrons. The capability was retained for the Van Allen Probes program because the electron detection feature is essential for monitoring background fluxes in the instrument.

Prior to an electron passing through the TOF head the electron is first decelerated by the 2.6-kV potential. The electron is later reaccelerated by 2.5-kV after exiting the head before reaching the SSDs. Energetic electrons from 25 keV to 1000 keV are measured by the electron SSDs. These detectors are covered with 2-μm aluminum metal flashing to keep out protons and other ions with energies less than about 200 keV. No TOF criterion is applied to the electron measurements.

4.2 Heritage

RBSPICE uses the measurement techniques and technologies demonstrated with the Galileo Energetic Particle Detector and the Geotail Energetic Particle Ion Composition instrument (EPIC), with a configuration similar to the New Horizons Pluto Energetic Particle Spectrometer Science Instrument (PEPSSI). RBSPICE is also nearly identical to the Jupiter Energetic particles Detector Instrument (JEDI) on the Juno Mission (launched August 2010).

The very similar PEPSSI sensor has the most relevant in-flight performance record to date, as it has provided high quality energetic ion composition measurements during the New Horizons Jupiter encounter. These data have demonstrated the capabilities of the TOF $\times$ E

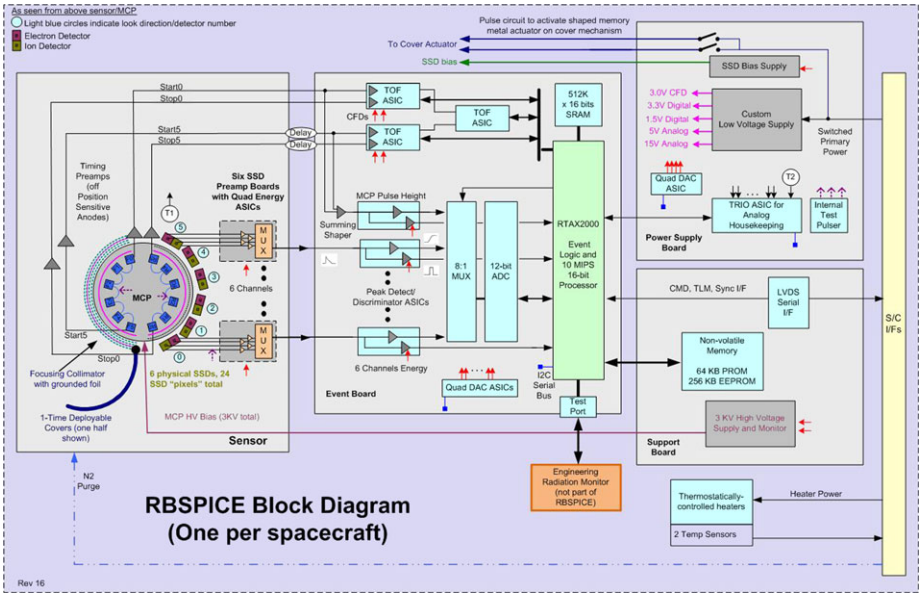

Fig. 7 RBSPICE block diagram

technique in rejecting penetrating energetic particle backgrounds while obtaining high quality ion composition and ion angular distributions. Figure 6 shows the PEPSSI flight instrument (upper left), energy spectrograms for protons, electrons, and heavy ions throughout the Jupiter flyby (upper right), and a TOF $\times$ E scatterplot demonstrating the capability of the instrument to resolve H, He, O, and S (lower left).

4.3 Block Diagram

Following the instrument block diagram from left to right in Fig. 7, the sensor generates analog representations of the particle TOF and SSD energy (left board in Fig. 7). The event board (center board in Fig. 7) directly processes the sensor SSD and anode preamp output signals, and contains all the necessary analog and digital circuitry to process and store event information on an event-by-event basis. Each SSD has an ion detector and an electron detector with both a large and a small pixel. There is only one analog electronics processing chain per SSD. Consequently, to collect both electrons and ions, the hardware is time-multiplexed between the electron and ion detectors. The energy signals from the six SSD preamplifiers and the MCP anode pulse height are processed in parallel peak-detect/discriminator ASIC chains feeding a multiplexed analog-to-digital converter (ADC). The MCP anode signals are processed via constant-fraction discriminators (CFDs) and time-to-digital (TDC) circuitry in the TOF ASICs. These measured time differences are converted into event look direction and particle velocity in the field-programmable gate array (FPGA). The FPGA-based event logic also determines which signals comprise valid ion and electron events and coordinates all event hardware processing timing. An RTX-2010 processor clone is embedded in the FPGA to provide all command, control, telemetry, and data processing functions of the instrument. SRAM and EEPROM support this processor. The software requires access to EEPROM and PROM infrequently so these memories are located on the support board (lower right board in Fig. 7).

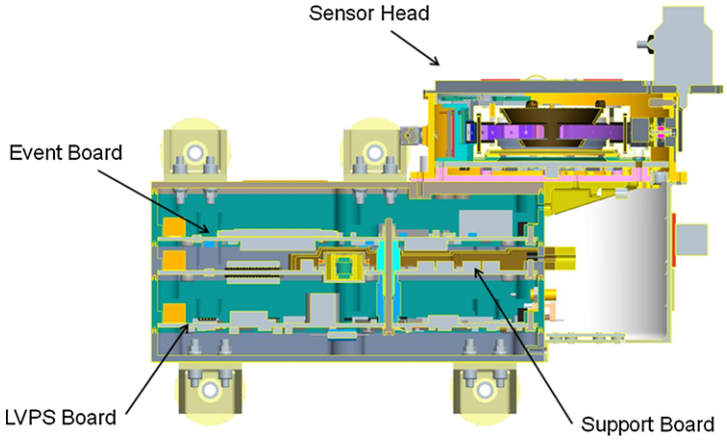

Fig. 8 RBSPICE cross section

In addition, the support board also contains the command and telemetry interface to the spacecraft. This board is designed to support either single-string or redundant LVDS or RS422 with part substitutions: for RBSPICE it is single string LVDS. The support board also generates the necessary high voltage outputs for the sensor MCP and electron optics up to 3300 V.

The power board (upper right board in Fig. 7) contains both the low and high voltage power supplies. The low voltage portion takes spacecraft primary power and generates 1.5 V (for FPGA core), 3.3 V (digital interface logic, memories, and TDCs), and 5 V (analog functions). A 15 V output powers the high voltage electronics on the support board. The power board also switches power to the sensor cover actuator mechanism, generates and filters 100 V bias for the SSD detectors, and uses a TRIO ASIC to measure currents, voltages, and temperatures.

4.4 Mechanical Configuration

RBSPICE is comprised of two subsystems: the sensor head and the main electronics box. The electronics box consists of three $4'' \times 6''$ printed circuit boards that are electrically connected with a custom 152 pin connector; the boards are stacked on top of each other (Fig. 8). The instrument housing is CuW in order to meet Van Allen Probes program radiation and deep dielectric discharge requirements. Total instrument mass is 6.6 kg. The sensor head and main electronics are mechanically integrated together and mounted as a single unit to the spacecraft (Fig. 9).

RBSPICE is mounted on a 16.9° bracket on the bottom spacecraft deck to have a clear FOV and prevent the sun from entering the FOV (Fig. 10). An additional 12° FOV is blocked in the collimator to accommodate sun off-pointing up to 27° Fig. 11). A door stop that prevents the sensor cover (Sect. 4.4.1) from fully opening permits the cover to provide additional sun blockage while not limiting the instrument field of view.

4.4.1 Deployable Cover

RBSPICE includes a deployable cover to prevent acoustic damage to the thin foils and to protect the sensor from contamination. The sensor cover mechanism consists of two curved,

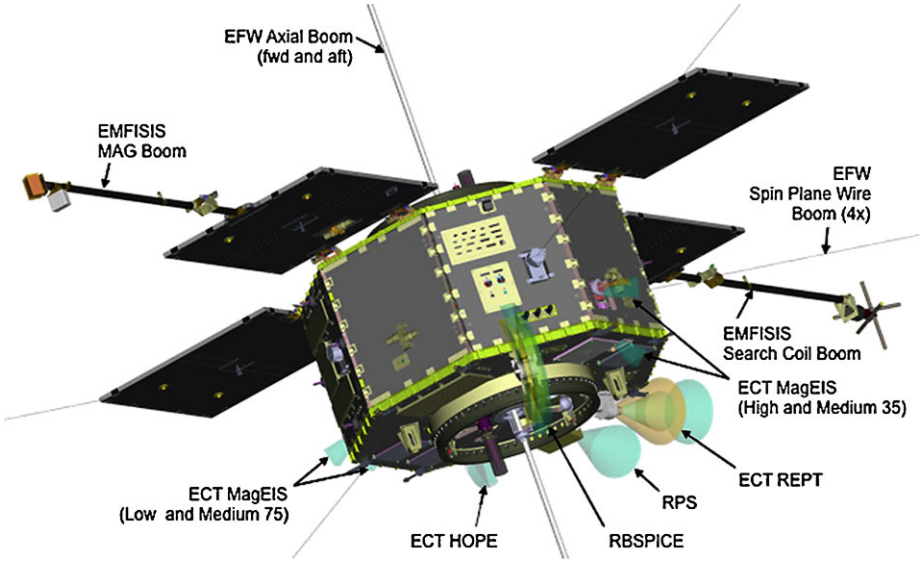

Fig. 9 RBSPICE placement on spacecraft

Fig. 10 RBSPICE on spacecraft mounting bracket

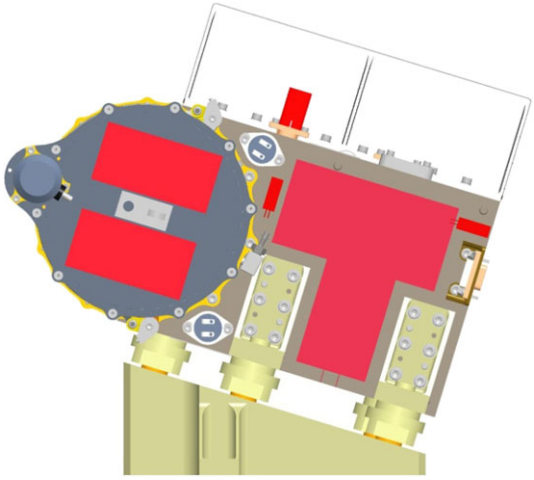

spring-loaded hinged doors that are retained over the aperture opening by a sliding pin. This pin can be pulled away from the doors (thus allowing the doors to swing free) via a pin-puller, shaped, memory actuator device. A sequence of three commands must be sent to fire the doors and, once opened, the covers are maintained in the open position by the springs. During ground testing, a safing plug also prevents accidental actuation; following ground testing activation, the doors are manually re-stowed.

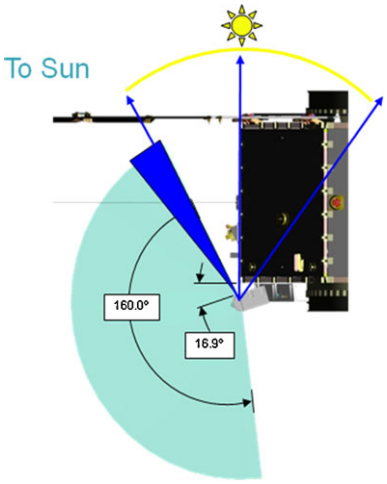

Fig. 11 Accommodation of sun off pointing

4.4.2 Thermal Design

The preferred RBSPICE operating temperature range is −25 °C to 0 °C with an acceptable operation range of −35 °C to +35 °C. The heat transfer between the spacecraft and the instrument is minimized by use of Multi-Layer Insulation (MLI) blanketing and thermal isolators on the mounting feet (Fig. 10). A radiator extension (shown to the rear of the instrument in Fig. 5) and a portion of the electromagnetic interference (EMI) shield serve as a radiator to allow RBSPICE to run colder than the spacecraft deck; a thermostatically controlled heater prevents the instrument from becoming too cold. RBSPICE survival temperature test limits are −40 °C to +60 °C.

4.5 Detectors and Foils

The RBSPICE sensor head and its component parts are shown in Figs. 12 and 13. The component parts are discussed in the following sections.

4.5.1 Microchannel Plates

Secondary electrons emitted by the start and stop foils are amplified by a pair of MCPs in the chevron configuration. Specifications for the individual plates are: 12 μm pore dia., $L/D =$ 60, 40 mm sensitive dia., 12 degree bias angle, 10–50 μA bias current, and output electrode penetration of ∼50 μm. The chevron pair was tested, baked, and scrubbed to .03 C/cm^2 by the manufacturer. The MCP was tested for gain, uniformity, and noise in the holder before incorporation in the next assembly step.

4.5.2 Solid State Detectors

Each SSD is 500 μm thick and segmented 4-fold on the particle entrance face. One half of the detector is optimized for ion detection by having a thin dead layer of ∼50 nm while the other half is optimized for electron detection by covering with 2 μm of Al to block ions below several 100 keV (Fig. 14). Each SSD half is segmented further into a small central pixel and a large surrounding pixel. The ratio of the large to small pixel areas is ∼20.

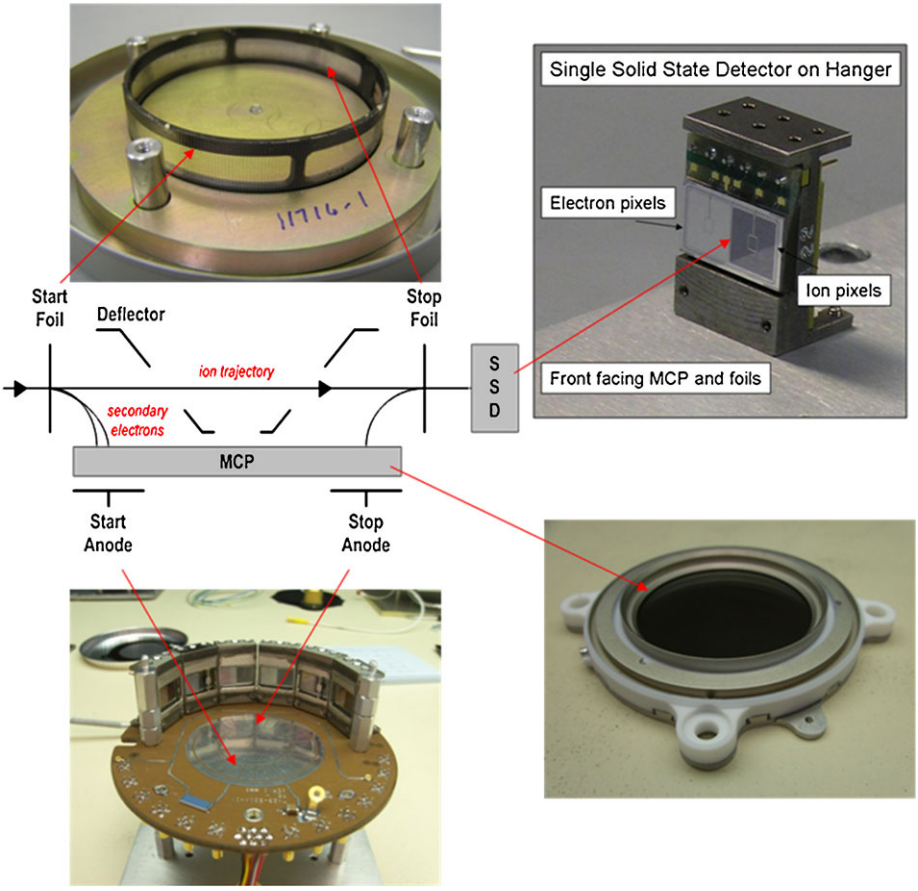

Fig. 12 Sensor components

4.5.3 Foils

The entry look directions are covered by two foils. The outer (collimator) foil is composed of two materials. 62 nm of aluminum covers the entire foil. The sunward-facing half of the foil is covered by an additional 17 nm of palladium to further filter solar EUV emissions. (Adjustments are made in the ground software tables in the RBSPICE Science Operations Center to account for the variable foil thickness as a function of the particle entry direction.) The inner (start) foil is a multilayer structure of 50 Å carbon/350 Å polyimide/50 Å carbon foil. The stop foil covers the exit aperture of the TOF section. It consists of a multilayer structure of 50 Å Carbon/350 Å Polyimide/50 Å C/200 Å Al. As discussed in Sect. 3.1, the collimator foil and the start foil reduce the UV photon background to the TOF section; the stop foil provides additional background reduction for the subsequent solid state detectors. The foils are supported by high transmittance (>80 %) metallic mesh. The start and stop foils are mounted on stainless steel frames while the collimator foil is mounted on a CuW blade of the collimator.

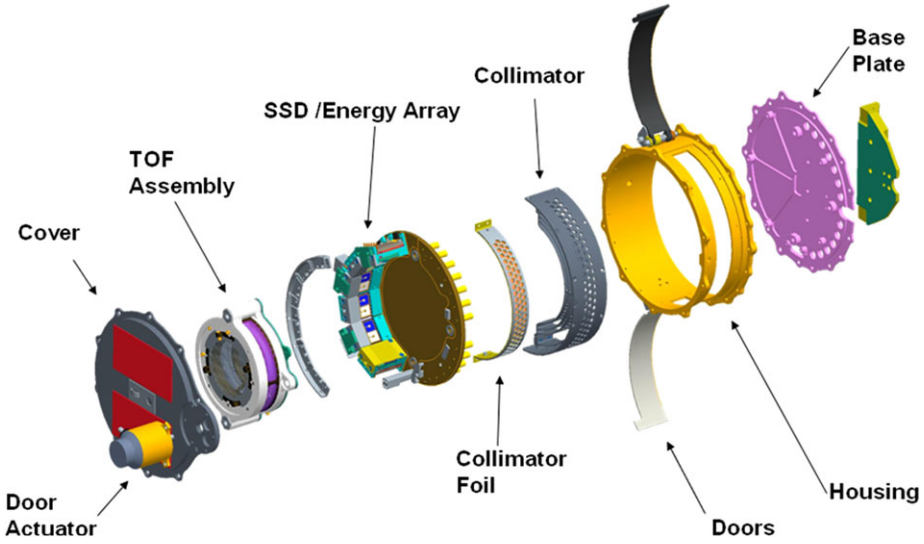

Fig. 13 Sensor exploded view

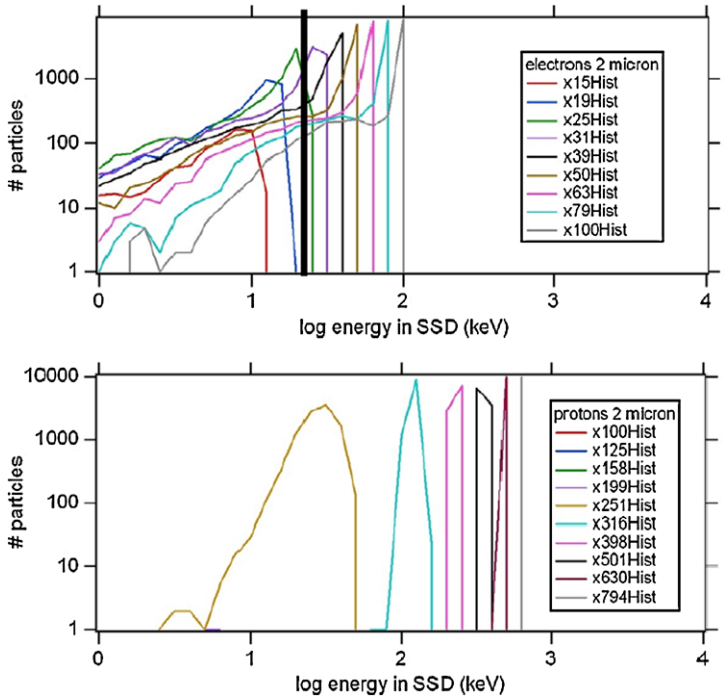

Fig. 14 The 2 micron aluminum flashing on the electron SSD pixels allows >25 keV electrons to be detected (*upper panel*) but strongly suppresses protons with $E < 300$ keV (*lower panel*)

4.6 Event Processing

4.6.1 Signal Flow from Detectors

Particle events stimulate the microchannel plates (MCPs) and solid state detectors (SSDs) as they pass through the sensor. MCP secondary electrons are mapped onto two 1-D position-sensing timing anodes. These anodes, the start anode and the stop anode, generate two timing pulses on each end of each anode. These four timing pulses are processed via the event processing board TOF-C ASICs to produce three timing words, corresponding to the time delay across the start anode, and two measurements of the particle time of flight. Some particles will be energetic enough to register in the SSDs. The derived energy measurement allows detailed categorization of the events; when no SSD signal is present, the MCP pulse height measurement is used.

4.6.2 Event Logic

The hardware is time-multiplexed between three possible modes: ion energy, ion species, and electron energy. The mode determines whether TOF or SSD pulses define an event. In the ion energy and electron energy modes, an SSD energy pulse starts an energy event collection. In the ion species mode, a TOF pulse starts an ion species event collection. Software controls the time-multiplexing of the hardware in order to maintain the illusion of independent electron and ion electronics. In general, RBSPICE does not enter the electron collection mode and time-multiplexes between only ion energy and ion species collection.

The event logic includes parameterized event selection criteria including individual SSD enable/disable, multiple event enable/disable, coincidence window length, and TOF validity flags required. In this way, processing of good events is maximized and noise counts have minimal impact (see Sect. 5.2).

The event processing logic passes valid particle event data to the software for further analysis. The events pass through a First-In First-Out (FIFO) within the FPGA. Each event consists of several parameters. For energy events, only SSD measurements and TOF coincidence flags are valid. For ion species events, TOF measurements and flags are also produced.

4.6.3 On-Board Data Structures

The RBSPICE software divides each spacecraft spin into 36 evenly spaced sectors. As the spin rate varies, the duration of a sector varies accordingly. The spin starts (i.e., sector 0 starts) when the inertial spin phase of the spacecraft is zero. Spin phase angle is zero when the sun line is in the $+Y$ half of the spacecraft YZ plane. The spacecraft provides spin period and phase data to RBSPICE. RBSPICE maintains an internal spin model by updating calculations based on the most recently received spacecraft spin data.

During periods of eclipse, the spin data become inaccurate. If the EMFISIS magnetometer is operational, RBSPICE can use the magnetometer data in lieu of spin data to maintain sector phasing. The RBSPICE software needs an interval when both spacecraft spin data and EMFISIS magnetometer data are valid so that the phase offset to one of the zero-crossings can be determined. If no spacecraft data have been received or if the data are invalid, a nominal 12 second spin period is used. On startup, it will take several spins for the internal spin model to eliminate its phase error with the actual spacecraft spin. Once the spin model and the actual spin are in phase, they will stay in phase as the spacecraft spin rate varies.

Fig. 15 Subsector timing

Table 3 Data products per hardware mode

Electron Energy	Ion Energy	Ion Species
Electron Energy Spectra	Ion Energy Spectra	Ion Energy Spectra and Proton (and Non-Proton) Rates
Basic Rates (Electron Energy)	Basic and Diagnostic Rates (Ion Energy)	Basic and Diagnostic Rates (Ion Species)
Raw Event Data (Electron Energy)	Raw Event Data (Ion Energy)	Raw Event Data (Ion Species)
		Priority Event Data
		Space Weather

Each spin sector is further divided into three subsectors. The first subsector is long, 1/2 of a sector. The last two subsectors are short, 1/4 of a sector each. This is illustrated in Fig. 15. As for sectors, the subsector timing varies with the spin rate.

The sensor hardware can be placed in a different mode during each subsector. The dark bars in Fig. 15 represent a fixed dead-time to switch between hardware modes: the first bar is ∼4.04 ms and the other two bars are ∼3.95 ms. The pattern of modes in each subsector is commandable. Any subsector may collect data in any mode. Each pattern collects different data in different proportions. For example, setting subsector 1 to ion energy and subsectors 2 and 3 to ion species collects ion energy 1/2 of the time and ion species the rest of the time; electron energy is not collected at all. If two adjacent subsectors have the same mode, there will still be a dead-time between the subsectors.

The data products (Table 3) generated by the RBSPICE software depend on the hardware modes commanded for each subsector. For example, if the electron energy mode is selected for all three subsectors, only electron energy spectra, basic rates, and raw event data will be collected.

The data products generated by the RBSPICE software are organized into three types depending on their integration time: fast, medium, or slow (Table 4). Slow RBSPICE data products can be integrated over multiple spins. At the end of its normal integration, if multi-spin integration is enabled, the data product is saved instead of being telemetered. When the spacecraft spin returns to the sector that began the product, integration resumes.

Each of the data products can be enabled or disabled by command. Data products will also be disabled automatically if they are not commanded. For example, if the ion energy mode is not scheduled in any of the subsectors, then Ion Energy Basic Rates will not be produced, regardless of its commanded enable or disable state.

Event analysis varies with the hardware mode, i.e., ion energy, ion species, or electron energy. For electron energy mode events, the RBSPICE software accumulates histograms of the SSD energy. Events are counted as processed by software and included in the basic rate data. Each event is also a candidate for inclusion in the raw event data. Ion energy mode events are processed similarly. For ion species mode events, the RBSPICE software accumulates ion species rate counts. Ion species events are either high energy with TOF and SSD energy measurements (Fig. 16) or low energy with TOF and PH (Fig. 17). Events are counted as processed by the software and included in the basic rate data. Each event is also a candidate for inclusion in the priority event data and raw event data.

Table 4 Data products per integration time

Type	Data Product	Integration Time (Sectors)	Multi-Spin?
Fast	Electron Energy Basic Rates	S	–
	Ion Energy Basic Rates		–
	Ion Energy Diagnostic Rates		–
	Ion Species Basic Rates		–
	Ion Species Diagnostic Rates		–
	Low Energy-Res./High Time-Res. Electron Spectra		–
	TOF × Energy Proton Rates		–
	Low-Res./High Time-Res. TOF × Pulse Height Proton Rates		–
	Priority Events		–
	Raw Electron Energy Event Data		–
	Raw Ion Energy Event Data		–
	Raw Ion Species Event Data		–
	Space Weather (Low Energy Counts)		–
Medium	TOF × Energy Non-Proton Rates	S*N1	–
Slow	High Energy-Res./Low Time-Res. Ion Spectra	S*N1*N2	Yes
	High Energy-Res./Low Time-Res. Electron Spectra		Yes
	TOF × Energy Ion Energy Spectra		Yes
	High-Res./Low Time-Res. TOF × Pulse Height Proton Rates		Yes
	Space Weather (High Energy Counts)		–

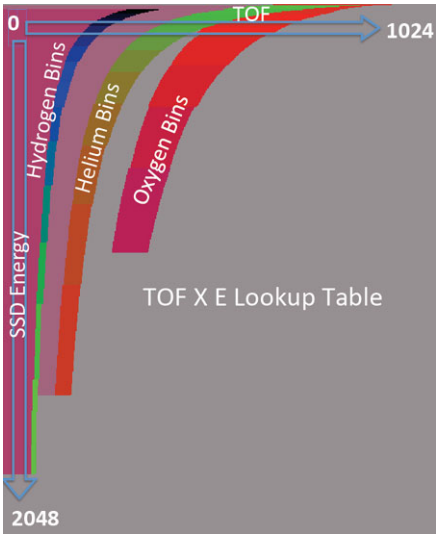

Fig. 16 TOF × *E* lookup table

The RBSPICE software measures basic event rates using hardware and software counters. The basic rates can also be used to automatically select the SSD pixel size. The RBSPICE hardware counts a variety of pulses from the detectors. In addition to valid particle events, these count foreground, background, and noise events. The valid events seen, as well

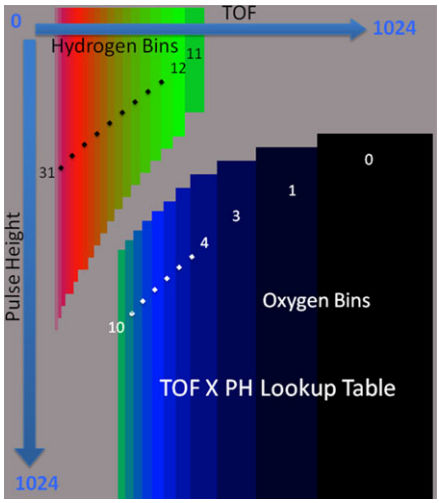

Fig. 17 TOF × PH lookup table

as the valid events placed in the FIFO, are counted. The software also counts the number of events it is able to process. The hardware counters are 24 bits. Every subsector, the counters are read out and accumulated in 32-bit counters in software. A different set of counters are collected in ion energy, ion species modes, and electron modes.

4.6.4 Engineering Radiation Monitor

The Engineering Radiation Monitor (ERM) monitors the total radiation dose received by the Van Allen Probes and is connected to the RBSPICE test port. RBSPICE software reads out one ERM value every second and telemeters the measurements every 3 minutes. RBSPICE also switches +5 V power to the ERM by command.

4.6.5 Diagnostic and Test Support

RBSPICE can inject pulses into the preamps of the TOF start, TOF stop, and SSDs to confirm signal flow through the instrument. The TOF start, TOF stop, and SSD pulses can be enabled or disabled individually by command. The rate of the pulses can be controlled onboard or with an external pulse generator during ground testing. The RBSPICE hardware can be commanded to measure SSD energy channel or MCP pulse height baseline values instead of doing its normal event processing.

4.7 Operational Modes

RBSPICE will normally be commanded on throughout the mission. The standard operational mode multiplexes the collection of ion energy data and ion species data including spectra, counters, and prioritized events. To further characterize the environment, RBSPICE also collects additional diagnostic counters, raw events, and electron energy data.

4.7.1 Boot Mode

During boot mode, RBSPICE supports commanding and telemetry but no macro services, monitoring, safing, or science collection. The boot PROM contains the start-up flight code.

4.7.2 Application Mode

Upon boot command, the flight software is copied from EEPROM into SRAM and the application code starts running. This standby mode has full operational capabilities without operational voltages and requires approximately 1.7 W. Additional commands configure the instrument with proper operational voltages, threshold settings, etc., to collect science data. In application mode, most processor time is spent analyzing event data and formatting telemetry. The processor is able to fully process 40,000 events per second. Full science operation requires less than 2.0 W.

5 RBSPICE Calibration and Performance

Various instrumental factors affect RBSPICE measurements, and all factors must be identified, evaluated, and accounted for prior to interpreting data. These factors include geometric factor of the instrument collimator, various foil thicknesses, and detector and electronics efficiency. These factors are identified and measured throughout the several steps of the instrument build, followed by a final calibration campaign before delivery. Continued instrument assessment in-flight is also used to evaluate all these factors.

Typical calibration procedure involves stimulating the instrument with energetic particles, first from laboratory radiation sources and later from accelerator beams, and recording the response of the instrument to the sources and beams. Calibration tests were conducted at the component, assembly and instrument levels. The functionality and response of the hardware was calibrated at each level to more completely understand the integrated instrument.

The detectors (SSDs, MCPs) were tested and calibrated individually with radioactive sources after arrival from vendors. The detectors were then characterized once again at the assembly level (sensor head, SSD array, etc.) as the flight build progressed. Finally, both flight instruments units were calibrated pre- and post-environmental qualification tests.

The combined calibration efforts focused on the following areas:

A. Collimator performance and geometric factor. The collimator and sensor geometry, and the size of the detectors, define the geometric factor (G) of the sensor. The multi-hole collimator design minimizes the scattering of ions and electrons in the collimator while restricting the FOV of the instrument. However, side lobes can exist in this collimator design. Simulation using the GEANT4 particle model and optical tracing software were used to assess the collimator performance for suppressing electron scattering and the rejection of scattered light, respectively.

B. TOF measurements. When the ions penetrate the start foil and enter the TOF section, secondary electrons are collected from both the start and stop foils by the MCP to measure the velocity of the ion. At low energy (tens of keV), ions lose significant amounts of energy and scatter significantly when going through the foils. Ion scattering, electron optics, and electronics all contribute to error in the measurement of time of flight. All these errors are identified and measured during the calibration.

C. Ion measurement. If an ion has sufficient energy once it transits the foils, it stops in a SSD. Depending on the final energy and mass of the ion, it will produce a measurable electronic signal in a SSD. However, both the dead layer and the pulse height defect of the SSD contribute to undetected energy loss, and both have to be both modeled, and measured during calibration.

D. Efficiencies. The total efficiency for detecting an ion involves combining scattering and consequent losses of ions within the front (collimator) and start foils, and secondary electron efficiencies for generating start and stop pulses to register a TOF within the maximum allowable time of flight window. The system efficiency is calibrated end-to-end for the entire sensor, including flight electronics.

E. Electron measurement. The RBPSICE electron measurement strategy depends on aluminum flashing over the electron SSDs, stopping ions below ∼300 keV. The effect of the flashing thickness on both the ion and electron energy measurements within the electron SSDs requires determination. Dedicated electron accelerator beam tests were used for this measurement.

F. Input rate vs. output rate characterization and photon rejection test. The RBSPICE instrument is tested to characterize its throughput as a function of increasing input flux. Visible and UV photon rejection is tested.

G. Background suppression. The flight-like engineering model unit was subjected to penetrating radiation tests at special high energy particle accelerator facilities (both electron and proton) to characterize the instrument background response in a high radiation environment such as the Earth's inner radiation belt.

5.1 Calibration Procedures and Facilities

A majority of the calibrations at the component and assembly level were performed using a set of National Institute of Standard and Test (NIST) calibrated alpha and beta emitters of known strength and energy. In addition, a custom-built source holder was made to fit onto the RBSPICE collimator that allows the simultaneous stimulation of the response of all RBSPICE detectors at the instrument unit level. During assembly level test, the RBSPICE flight model sensor heads were calibrated both at the APL accelerator facility (ions between 12 and 170 keV) and at the NASA Goddard Space Flight Center (GSFC) Van de Graff Accelerator facility for electrons and ions from 125 keV to 1.6 MeV. The APL particle accelerator is capable of producing beams of H, He, O, N, Ne, Ar with intensities from 10's to 1,000,000 particles/cm^2/s. The accelerator target chamber is custom outfitted with a 4-axis articulation stage designed to accommodate RBSPICE such that all look directions within the instrument field of view can be exposed to the accelerator beam.

5.2 RBSPICE Capabilities Versus Requirements

RBSPICE Level 3/4 science requirements drive the calibration requirements. Particle intensities must be known to relative/absolute accuracy of 20 %/50 %. The RBSPICE calibrations fully satisfy the Level 3 requirements in all areas, and frequently exceed those demanded from the project requirements.

As noted above, RBSPICE is essentially identical to the JEDI instrument on the Juno spacecraft destined for Jupiter, with exceptions for mechanical and accommodation details such as thermal surfaces, data interfaces, collimator field of view, and collimator foil thickness and composition. All of the calibration scopes and procedures described were determined by the JEDI project. Since the instruments on the Van Allen Probes and Juno spacecraft are nearly identical, much of the RBSPICE characterization could be achieved by calibration results derived from the JEDI program.

Since identical start and stop foils are used in both programs, the efficiency of the TOF measurement as a function of species and energy is expected to be the same for the two instruments. Figure 18a shows fits to the calibrations of efficiency for various species and

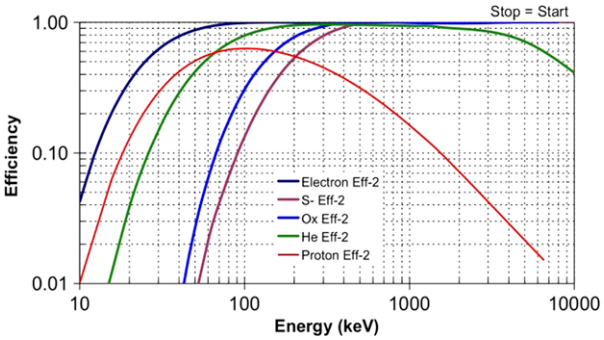

Fig. 18a Fit efficiencies vs energy for various species for required Start position = Stop position

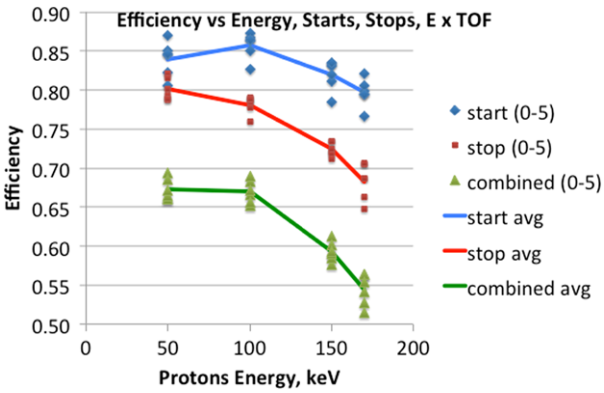

Fig. 18b Measured proton efficiencies for Start = Stop

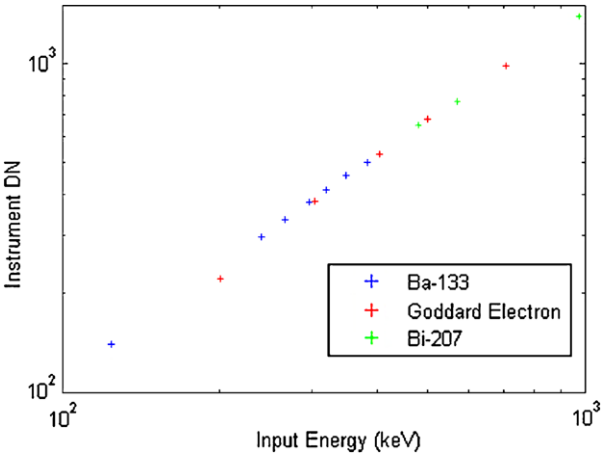

Fig. 19 Calibration of RBSPICE SSD response, Data Number (DN) corresponding to input electron energy in keV

energies under the requirement that the Start position equals the Stop position (meaning the scattering in the Start foil is small enough that the particle crosses the TOF region roughly on a diameter). Figure 18b shows the detailed efficiency (start, stop and total) measurements for protons at different energies on JEDI for $E \times$ TOF under the requirement that Start = Stop positions. On RBPSICE, the efficiencies for several energies were spot-checked, validating the adoption of the JEDI results for RBSPICE.

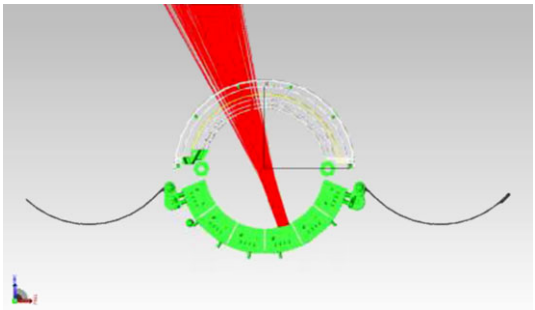

Fig. 20a Subset of isotropic rays leaving the surface of SSD 3 that get out through the collimator

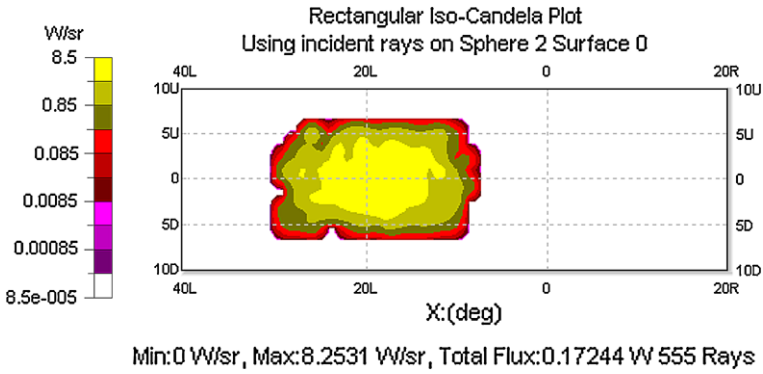

Fig. 20b Angular distribution and relative intensity of rays shown above

Figure 19 shows the calibration of RBSPICE between input energy and data number (DN). Because electrons lose negligible amounts of energy in passing through the foils and dead layers, two beta sources and multiple electron beams from GSFC were used to cover the entire energy range of the instrument.

The results of measurements that establish the RBSPICE capabilities are the following:

A. *Collimator performance and geometric factor.* The sensor geometric factor was established by two methods: (a) modeling the CAD model of the sensor for its reverse optical paths from the solid state detectors out through the collimator (Figs. 20a, 20b), and (b) actual measurement (both through sweeping the sensor over a range of angles relative to an incident ion beam, and by covering the sensor collimator aperture with a distributed, omnidirectional alpha source that fully covers all of the collimator entrance holes, and recording the relative responses for each angular bin). The first method uses the instrument geometry as captured in the instrument CAD model and computes all possible ray paths from the detector and foil surfaces outward through the collimator. This not only directly determines the solid angle that each surface element of a detector views, but at the same time systematically searches the model for possible side lobes/light leaks. The CAD reverse ray tracing does not include efficiency factors introduced by start and stop foil secondary electron production efficiency (which is a function of species and energy).
Calibration using the distributed alpha source on the collimator aperture includes the start and stop foil efficiencies (since it is an actual measurement of particles), as well as scattering losses and impacts with the grids that support a given foil. For high-energy alpha particles, the secondary electron generation efficiency is quite high and scattering in the

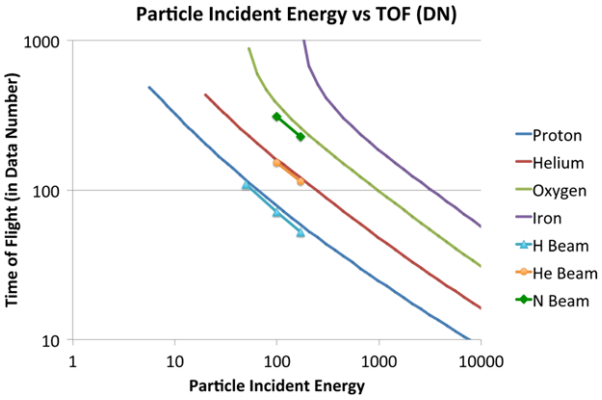

Fig. 21 GEANT4 model of particle incident energy vs TOF in DN, based on modeled energy loss in front and Start foils. Data points from accelerator beam runs are included for comparison with the predicted curves

foils is very low, so most of the differences between the optical modeling and the measurements can be attributed to impact losses of the alpha particles in the foil support grids. The alpha particle measurements also allow estimation of the relative geometric factor between TOF-only and TOF $\times$ E measurements (the TOF-only geometric factor is nominally about a factor of 2.5 times larger than the TOF $\times$ E geometry factor for the large pixels, and about a factor of 50 larger for the small pixels).

B. TOF measurements. When ions penetrate the start foil and enter the TOF section, secondary electrons are collected from both the start and stop foils onto the MCP to measure the velocity of the ion. At low energies (tens of keV), ions lose significant amounts of energy and scatter significantly when going through the foils. Ion scattering, electron optics, and electronics all contribute to error in the measurement of the time of flight. GEANT4 modeling has been done for both the energy losses and the scattering of ions as a function of energy and species to produce predicted RBSPICE TOFs and SSD energies. The results of ion beam and alpha source measurements have been cross-compared with GEANT4 predictions, and the two methods have been found to be in close agreement. Figure 21 indicates the mapping between ion incident energy and the TOF predicted to be measured by the instrument, expressed in data number (DN, which is what is used in-flight to determine the ion velocity). Data points derived from APL Accelerator runs are also included for a few energies. Generally, these results are quite consistent with the predicted curves. In particular, the He data agree very closely; the H data fall slightly below the predicted curve, a departure also observed in the flight data. A correction to the species lookup table on the flight instruments corrects this small departure. Oxygen beam data are not available, but nitrogen beam data have been obtained. These nitrogen data fall below, and nearly parallel with, the oxygen curve, as they should.

Below a species-dependent lower energy bound, ions do not have sufficient energy to generate a signal above a SSD detector threshold. The RBSPICE instrument classifies such ions broadly as either hydrogen or oxygen according to the TOFs and the MCP pulse heights. The third most common magnetosphere ion (helium) can be classified as either species, but is more likely to be either classified as hydrogen or rejected. As RBSPICE is not required to identify helium uniquely at energies lower than 70 keV total energy, these misclassified helium ions simply contribute to uncertainty in the hydrogen and oxygen intensities. However, as the abundance of helium is typically low relative to hydrogen or oxygen, this uncertainty is not important for RBSPICE measurement requirements.

C. Ion energy measurement. If an ion retains sufficient energy once it transits the foils, it will stop in a SSD. Depending on the final energy and mass of the ion, it will produce

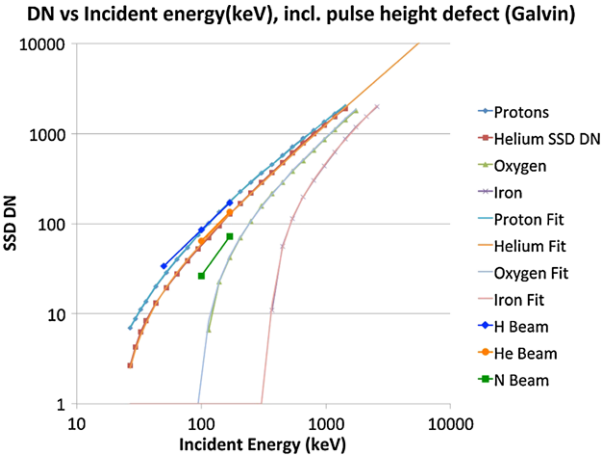

Fig. 22 Curves of particle incident energy versus SSD output Data Number (DN), including modeled energy losses in the front, Start, and Stop foils, in the SSD dead layer, and detector pulse-height defect. Individual points are for discrete energies modeled in GEANT4, curves are fits to those points to allow interpolation to energies not modeled. Data points from accelerator beam runs are included for comparison with the predicted curves

a measurable electronic signal. However, losses in the foils, SSD dead layers, and pulse height defects of the detectors contribute to undetected energy loss. These energy losses are modeled in GEANT4, whereas the pulse-height defect is taken from work by Galvin (private communication). Figure 22 shows the curves for the predicted SSD response (in data number) for a broad range of input energies. Data points from accelerator beam runs are included for comparison. The nitrogen points were measured as a proxy for oxygen, but fall above the oxygen curve as they would be expected to. In general the data agree very closely with the predictions, although there is a tendency for the measured SSD DN to lie above the predictions at lower energies, near the SSD electronic threshold. This is a threshold effect caused by electronic noise, and it has been taken into consideration in the generation of the TOF $\times$ E lookup tables on the flight instruments.

By combining the results in Figs. 21 and 22, the data number (DN) measurements of energy and TOF can be predicted for each species over the RBSPICE energy range. These results are used to construct the TOF $\times$ E lookup table that resides in instrument memory, and by which the DPU assigns the measurement to a particular species. At energies below which the SSD pulse is under threshold, the MCP pulse height is used together with the TOF to assign species via an onboard lookup table. The results of this procedure are captured in Fig. 23a, which shows the classification by the RBSPICE Flight Model1 of calibration data from a degraded alpha source.

Although a small fraction of the particles produce anomalous energy signals, accounting for the out-of-track haze in Fig. 23a, the vast majority of the particles lie along the expected track. The points in red are events that have been classified by the RBSPICE TOF $\times$ E lookup table as being helium events. The lookup classification very successfully eliminates events with spurious parameters from the helium rate bins. The lookup table only extends up to 400 keV, the upper limit for the required helium rate bins in the telemetry. The inset in the upper right of Fig. 23a shows the mapping of events into specific telemetry rate bins, verifying the energy bounds of the helium rate bins (red oval) in flight software.

A small number of events (a small fraction of the scatter in Fig. 23a) are misidentified by the lookup table as hydrogen, and these events are binned into hydrogen rate bins (blue circle). Although this means that in flight a small fraction of the measured helium will be misclassified as hydrogen, the ambient magnetosphere hydrogen will outnumber these few misclassified events by at least 4 orders of magnitude at any particular energy, rendering the misclassified particles negligible. The remaining events are classified as not belonging

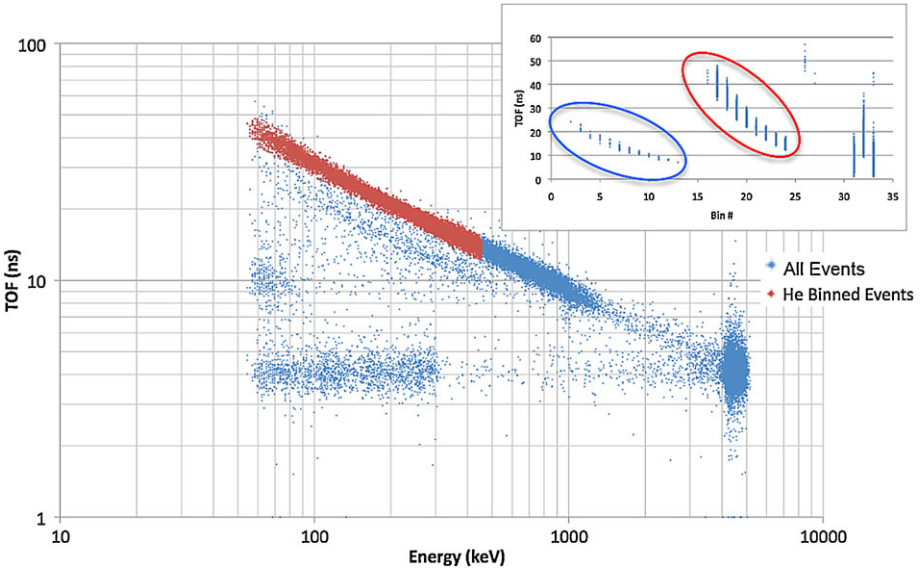

Fig. 23a Scatter plot of events (TOF × E) from degraded alpha source, RBSPICE FM1. *Inset* plots the mapping of the points in the scatter plot into the species energy bins as determined by the flight software lookup tables (protons bins 0–14, helium bins 15–25, oxygen 26–30, and "other" 31–33)

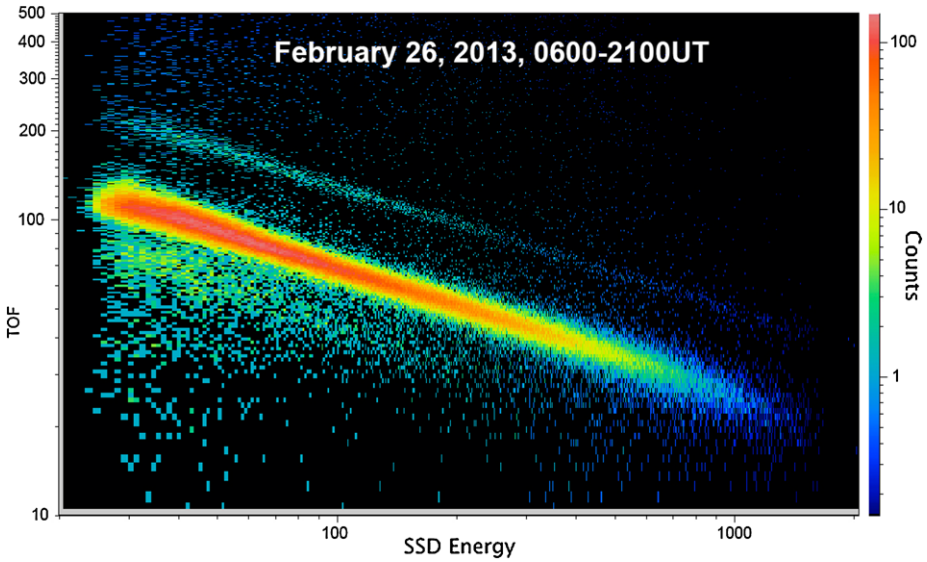

Fig. 23b Scatter plot of events downloaded from RBSPICE-B in flight, day 331, 2012. The brightest track is hydrogen, the faint track is helium. Oxygen is nearly absent, with only a few points in the location of its track

to any of the lookup table identifiable species, and these are binned into non-science rate bins; these are also telemetered to keep track of the fraction of events that are not valid according to the flight software algorithms. The large number of points near 5 MeV comes

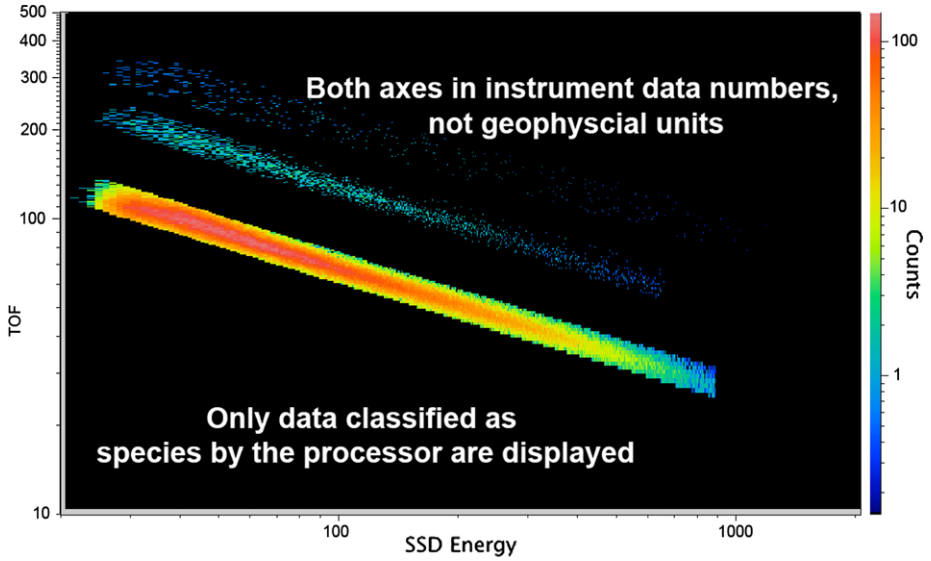

Fig. 23c Same as Fig. 23b, but only including data binned into defined species bins (i.e., bins 0–30; see Fig. 23a). This plots shows that the bin definitions for hydrogen are slightly off, and the hydrogen track is being clipped at high energies (resulting in lower efficiency for those spectral bins). This has since been corrected with a new lookup table

from a portion of the area of the alpha particle calibration source that was not degraded. Figures 23b and 23c show examples of the in-flight performance of RBSPICE B (FM2), and Fig. 23d shows an example energy spectrogram during an energetic particle event seen on orbit for RBSPICE B (FM2) showing electrons in the top panel and ions in the bottom panel.

D. Efficiencies. The total efficiency for detecting an ion involves the combined scattering and consequent losses of ions within the three foils, and secondary electron efficiencies for generating start and stop pulses to register a TOF within the maximum allowable time of flight window. Proton energy efficiencies are shown in Figs. 24a, 24b, 25a and 25b.

E. Electron measurement. RBSPICE has no formal measurement requirements for electrons. However, as discussed above, electrons represent potential sources of background for the ion composition measurements. Furthermore, electron calibration of the SSDs is a necessary step in determining the mapping between keV and DN in the instrument. Example electron calibration data are shown in Figs. 26a, 26b.

F. Input rate vs. output rate characterization and photon rejection test. The RBSPICE instrument was tested to characterize its throughput as a function of increasing input particle flux, and visible and UV photon rejection (Fig. 27). The RBSPICE package includes a large number of hardware and software counters that track detector singles rates, various coincidence rates, state machine idle time, various component dead times, etc. Using these housekeeping data, calibrated intensities can be recovered in spite of various bottlenecks in the sensor through-put at high rates. Such high rates were not generated in accelerator tests for a variety of reasons, most simply understood in considering that with the curved collimator composed of radially aligned paths, the accelerator beam could only enter through a very small fraction of the collimator at any one measurement geometry. Although accelerator rates could be driven fairly high, saturation effects of the MCP, and overdriving of the

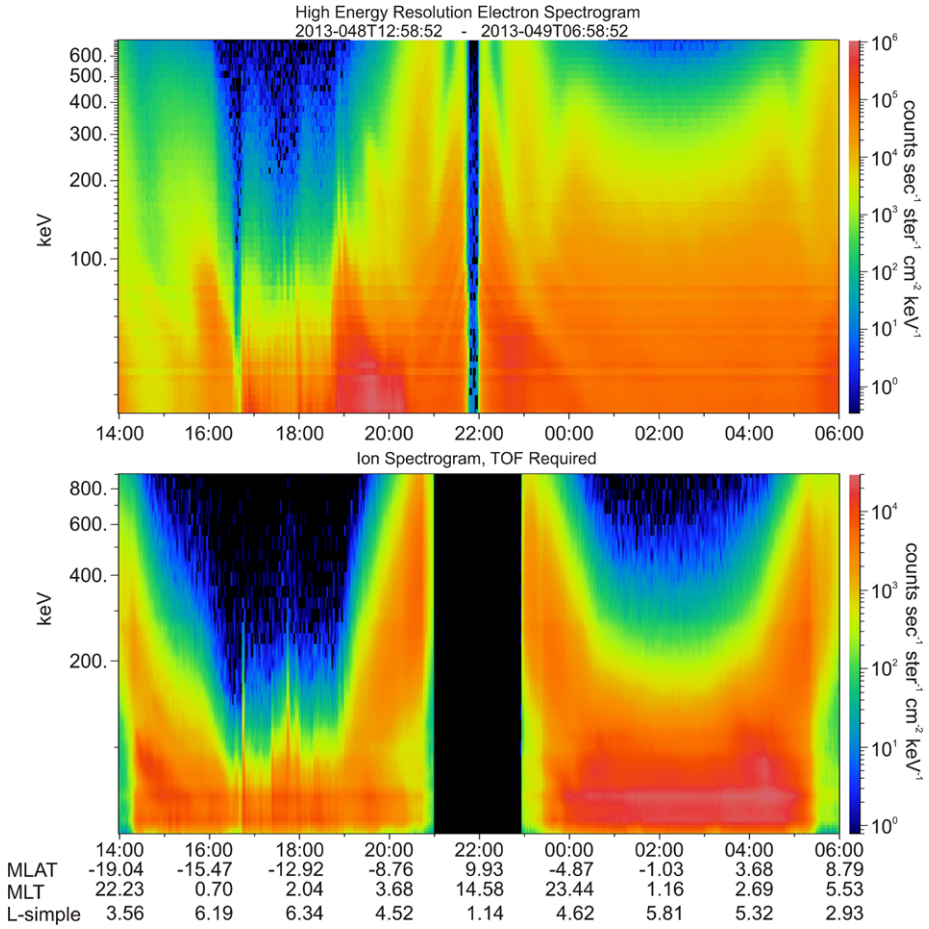

Fig. 23d Example of in-flight energy spectrogram from the detectors showing electrons (*top panel*) and ions (*bottom panel*). The intensities are actually dominated by electrons; ions are cleanly extracted by requiring a TOF, so that the much lower ion intensities represented in Figs. 23b and 23c can be measured in the presence of these electrons

SSD while the other SSDs were not seeing any flux, leads to very unrealistic conditions and in fact does not allow for driving the FPGA logic at particularly high rates. Such high rates are quite readily driven in flight, with all collimator angular directions filled with high intensities. Therefore, high rates were achieved through pulser stimulation of the front-end electronics instead, and it is those results that are shown in Figs. 27, 29, 30, and 31.

G. Background suppression. The flight-like RBSPICE engineering model unit was subjected to penetrating radiation tests at special high-energy particle accelerator facilities (both electron and proton) to characterize the instrument background response in a high radiation environment.

5.3 In-Flight Calibration

In-flight calibration is conducted as needed. The calibration telemetry modes include several data products not normally telemetered, as well as higher time resolution for some data

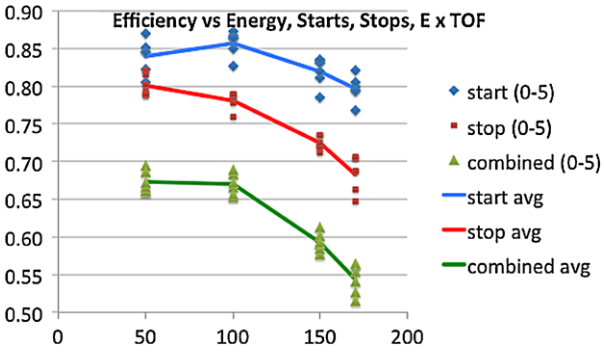

Fig. 24a Efficiency for protons, $E \times$ TOF

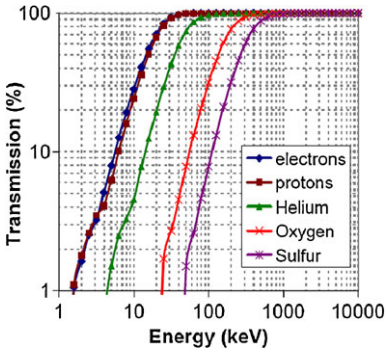

Fig. 24b Transmission as a function of species and energy, losses dominated by scattering in the front (collimator) foil

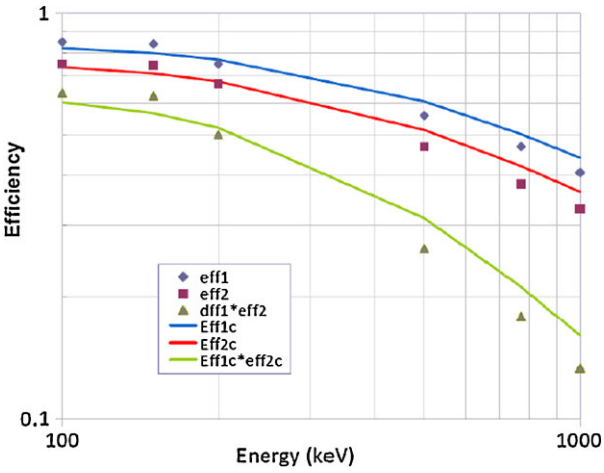

Fig. 25a Proton efficiencies above 100 keV, with functional fits to those efficiencies

products. Among the products that can be included during calibration intervals are diagnostic rates (which include additional information on state machine dead-times, etc.) and raw event data (which provide additional information on various low-level quantities that the instrument typically uses internally to calculate higher level quantities such as energy, time of flight, and species). Depending upon the goals of a calibration, various telemetry modes are available. All of these modes produce data at a higher rate than would fit within the RBSPICE downlink allocation data volume were they to be used continuously. Some modes

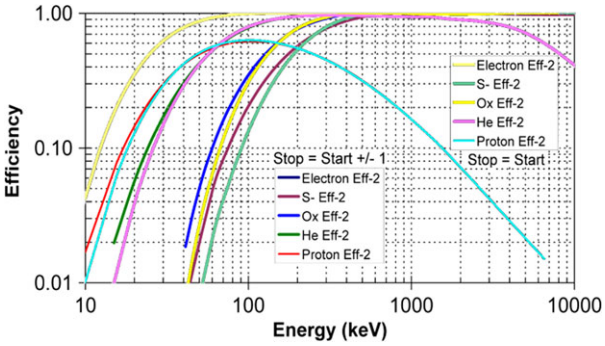

Fig. 25b Fits to over-all efficiency, including secondary electron effects as well as front foil scattering effects. The curves separate at low energy according to valid event logic, i.e. whether the Stop position is required to be equal to the Start, or whether Stop can be within 1 above, equal to, or 1 below the Start position. The latter are modified for positions at the extreme ends of the position chain (since only +1 or −1 is available there)

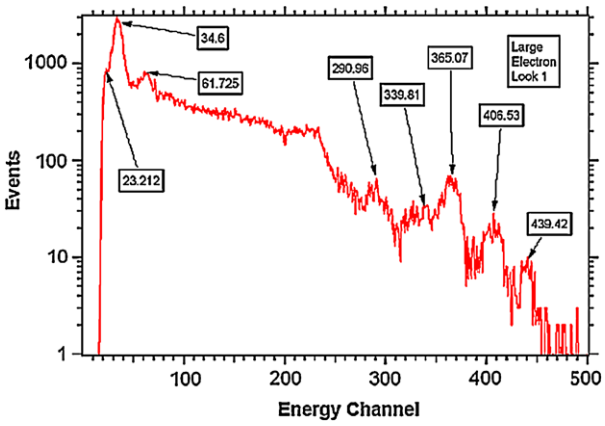

Fig. 26a Calibration of the RBSPICE energy measurement with radioactive sources (Ba133 and Bi207) together with monogenetic electron beams

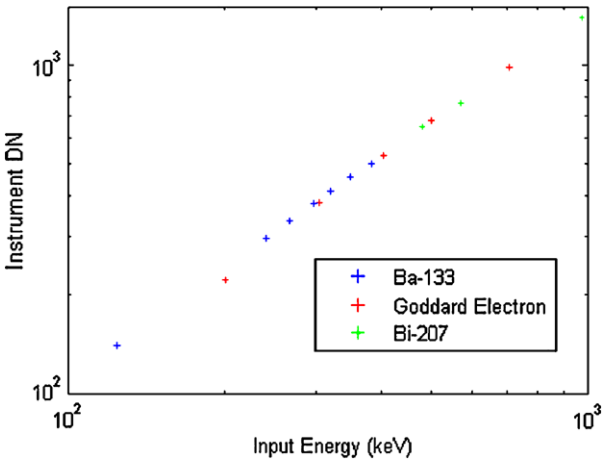

Fig. 26b Linearity of the RBSPICE energy response from 100 keV to 1 MeV

produce only slightly more data (for example, Checkout Mode) whereas others produce up to and more than four times the nominal allocated rate. Therefore, these modes will be used selectively and sparingly during flight.

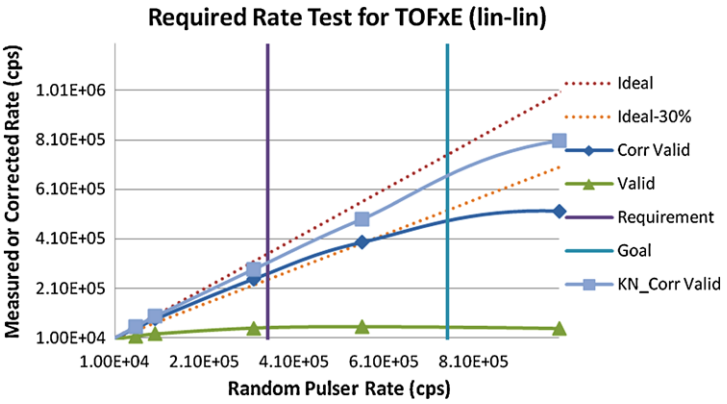

Fig. 27 Data from bench test demonstrating the correction of output rates to match the input rates using instrument-reported idle times and dead times. Output rate corrections are good to about 10 % for input rates to more than 8×10^5

During calibrations, on-board pulsers may be exercised to stimulate the sensor front-end electronics, depending on the goals of the calibration.

A principle concern is determining and setting the efficiency of detection of secondary electrons coming from the start and stop foils, given the changing gain states of the MCP's over time. This is also a concern for the nearly identical JEDI sensors on Juno, and the following paragraphs are excerpted from the JEDI instrument paper to describe how this important consideration is handled. There are two features of RBSPICE that make this process much easier than it has been on heritage instruments. The first feature is that complete detailed pulse height distributions (2048 channels) can be obtained in flight for the start region of the MCP, allowing the detailed response of the start system (start foil, MCP, anodes) to incoming particles. To take advantage of this capability, the so-called event data must be telemetered to ground. The complete diagnostic event data can be sent, but generally to preserve telemetry volume a subset of that information is sent. With several hours of sampling, the individual event data may be sorted according to energy, TOF, Pulse-Height (PH), and look direction, and so the PH distribution for a "standard candle" energy (e.g. 100 keV protons) for each look direction can be generated and compared with ground distributions and with other distributions in space. Because the pulse height distribution is obtained only for the start pulses, this procedure only diagnoses the evolution of secondary electron detection of the start region, not the stop region. However, the start region is where the more rapid changes in efficiency are expected due to the greater flux of particles and UV light onto the start foil than is expected on the stop foil (the geometric factor of just the start foil is a factor of 3–4 greater than the geometric factor of just the stop foil).

The second feature that RBSPICE contains to determine the efficiencies of secondary electron detection, for both the start and the stop regions, is the ability to count various kinds of coincident events. If by choice only "diagnostic rates" (generally not sent to the ground in order to save telemetry) are telemetered, there are counters that report coincident SSD-Start counts and coincident SSD-Stop counts. Total TOF-SSD counts (non-directional), and under some conditions (at relatively low rates) directional TOF-SSD counts can also be reported. These counters can be combined to obtain the efficiencies of secondary electron generation for both the start regions and the stop regions.

The principal responses to changes in the efficiency of secondary electron generation are: (a) to increase the gain of the MCP by increasing its bias voltage, and/or (b) to modify the TOF × PH look-up tables by adjusting a multiplicative parameter.

6 RBSPICE Sensor Operations

The RBSPICE instrument will typically be operated in a single science mode throughout the flight mission. Depending upon in-flight experience, and in order to avoid unnecessary premature aging, during inner radiation belt transits the MCP high voltage may be reduced below the level where the MCP multiplies signals. Periodically (approximately once per month) the instrument will be commanded through a calibration sequence, involving internal pulsers and high resolution diagnostic data modes (Sect. 5.3). Detector status will be tracked (noise levels, MCP pulse-height performance), and any necessary adjustments will be made to thresholds and voltage levels to keep the instrument within its calibrated response.

Downlink health and safety data from the instrument housekeeping data stream, as well as relevant spacecraft housekeeping data will be tracked and reviewed daily. Science data is converted to browse products and will also be examined as an indicator of instrument health and calibration status.

Command loads to maintain proper instrument state will be generated, tested on the Engineering Model, and uploaded as required. This will nominally be no more frequent than once per week.

7 RBSPICE Data: Reduction, Products, Distribution, and Archiving

7.1 Overall RBSPICE Data Handling

An overview of the data flow to and from each RBSPICE instrument into the RBSPICE Science Operations Center (SOC) is provided in Fig. 28. As the diagram indicates, data operations are broken into two specific segments: Commanding and Data Processing, each operating out of different RBSPICE SOC facilities.

Commanding occurs through the spacecraft tracking facilities in the Space Department at Applied Physics Laboratory (APL), where a workstation runs the Ground Support Equipment Operating System (GSEOS). This GSEOS is specifically tailored for the Van Allen Probes mission and managed by the Van Allen Probes project. One workstation is dedicated to each of the two RBSPICE instruments.

Commands are created, tested, and verified against the Spacecraft Emulator and the RBSPICE Engineering Model (EM). Once validated, command sequences are added to a standard commanding library and are available for later use as needed. All commands are sent as CCSDS packets to the Van Allen Probes Mission Operations Center (MOC) through interfaces between the RBSPICE SOC at APL and the Van Allen Probes MOC. (The interfaces are specified in the Van Allen Probes Interface Control Document (ICD) entitled 7417–9050 MOC to SOC). During contact times, the MOC will telemeter the command(s) to the targeted spacecraft. Validation of execution of the commands will be seen in subsequent telemetry received from the instrument (see below specific data products).

Data processing occurs primarily through servers running at Fundamental Technologies (FTECS). The data system is configured to be as automated as possible, providing the means to directly download RBSPICE telemetry for each spacecraft to the RBSPICE

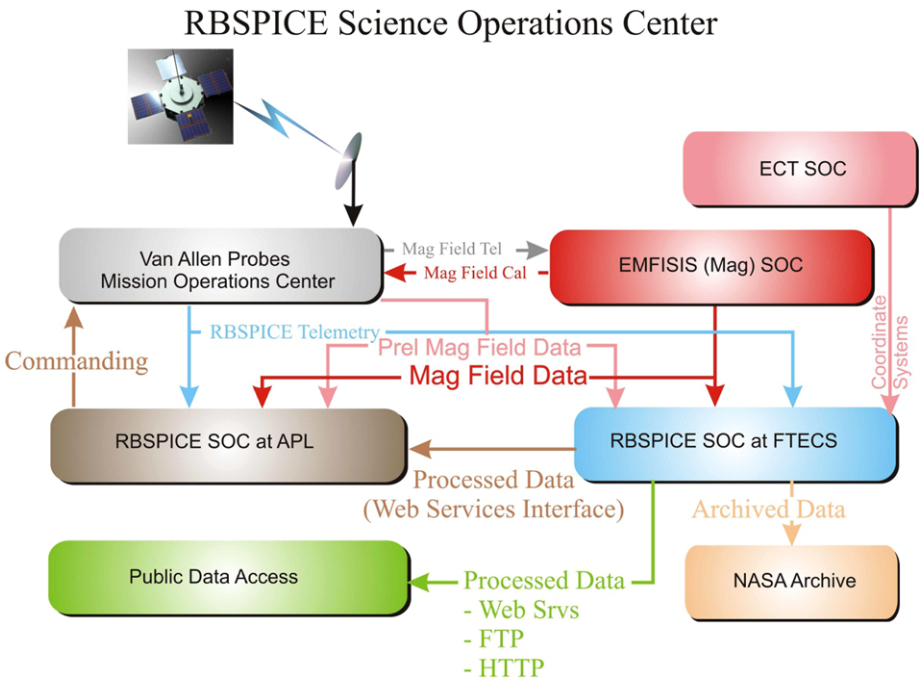

Fig. 28 Schematic diagram of RBSPICE data acquisition and flow

SOC operations at FTECS. In addition, magnetic field data from the EMFISIS instrument is downloaded to the RBSPICE SOC at FTECS to enable the calculation of particle pitch angle-related data products. Finally, the RBSPICE SOC acquires the ephemeris for each spacecraft from the MOC but also acquires spacecraft coordinate system data using various magnetic field models as calculated by the ECT SOC. Coordinate system information is included in the RBSPICE Level 2 and higher data products. Telemetry and other data, such as the magnetic field data, are then categorized and analyzed based upon specific Application ID's (APID) for each product. Each APID is then processed into either auxiliary support information or higher-level data products. Redundant operations are maintained in the Space Department at APL, in the event of significant internet connectivity failures during mission operations. The final RBSPICE data products are hosted at FTECS on a web server, allowing for public access to the data with very short lags from reception of telemetry data to final data products.

The TOF/SSD-based RBSPICE instrument provides a large number of data products based upon specific commanding options provided to the instrument. Table 5 provides a high level summary of the various data products produced in the RBSPICE SOC. All but the raw telemetry will become publicly available through the RBSPICE SOC web site within the latency time frame as identified in the table. The Level 4 data products will only be produced for selected ring current events and are not part of the automatic data processing system. These Level 4 products will be generated through other science software and made available through the RBSPICE SOC web site as the products become available. Each of the data products will be provided as a self-describing CDF formatted data file, as well as an ASCII Comma Separated Value (CSV) data file.

Table 5 RBSPICE data products

Data Level	Product Title	Contents	Daily Volume	Format	Latency	Frequency
L0	Raw telemetry	Raw de-commutated telemetry received at RBSPICE-SOC	~414 MB	Binary, ISTP Compliant CDF & ASCII (CSV)	from Receipt (T_0)	daily
L1	Count Rates	Sorted, time-tagged, instrument separated counts/sec	~750 MB	ISTP Compliant CDF & ASCII (CSV)	$T_0+ < 14$ days	daily
L2	Calibrated Flux	Calibrated and corrected physical units	~1200 MB	ISTP/PRBEM Compliant CDF & ASCII (CSV)	$T_0+ < 1$ month	daily
L3	Pitch Angle and Moments	Pitch angle distributions, 1st adiabatic invariant	~1500 MB	ISTP/PRBEM Compliant CDF	$T_0+ < 3$ months*	daily
L4	Phase Space Density	PSD units, 2nd and 3rd adiabatic invariants, magnetic coordinates	~30 MB	ISTP/PRBEM Compliant CDF	$T_0+ < 1$ year	Selected events

Table 6 lists the data products that can be directly related to the particle counts measured by each of the RBSPICE instruments. The data products are organized by the type of product, the particle species, and the NASA data level.

In general, the basic rate and diagnostic rate data, as well as the auxiliary and critical housekeeping data, are used to guide the production of the other data products. This includes the understanding of cases of very high rates where the Rate_{In} versus Rate_{Out} (R_{In} vs R_{Out}) calibration has to be taken into consideration (Sect. 7.2). The basic rate and diagnostic rate data are produced as rate and flux data, but users will find those particular products less helpful in understanding the overall Phase Space Density distributions (PSD) of the source populations.

Each of the data products are organized by either the Mission Elapsed Time (MET) or the Ephemeris Time of the measurement. The products are also organized by the spacecraft orbit number, spin number, and by the sector number with which the measurement is started. The duration of a measurement for each product is programmable. This permits lower energy products with higher particle counts to be measured over shorter periods of time and higher energy products with much lower particle counts to be measured over longer periods of time.

A description of each of the higher level data products and the controlling variables for the duration is listed in Table 7. Additionally, this table provides short product names mapping from the longer names that relate to how the overall directory structure is organized. The duration variables are S measured in the number of sectors, N1 and N2 as multiplying factors, and "spins" representing the number of integration spins. That is, if a product is identified to have a measurement duration

of S*N1*N2, then the measurement of the product will start in a particular sector and stop at S*N1*N2 sectors later. For products that allow for multiple spins, the measurement from the start sector to the stop sector is repeated for a total of "spins." Each of the S, N1, and N2 variables is configurable in the flight software with the following limits: $1 \leq \text{S} \leq 36$, $1 \leq \text{N1} \leq 36$, and $1 \leq \text{N2} \leq 36$. In general, the values of S, N1, and N2 are used to manage the overall telemetry rate of the RBSPICE data. Using this formulary, the highest energy data products can be measured over multiple spins allowing for better statistics in the data collection, but sacrificing some understanding of the pointing of the instrument.

Table 6 Detailed RBSPICE data products

Product	Species	Energy Bins	L0 Data Type	L1 Data Type	L2 Data Type	L3 Data Type	L4 Data Type
Low Energy Resolution High Time Resolution Electron Species Rate	Electrons	14	Count	Spectra Rate	Spectra Flux	PAD, μ	
High Energy Resolution Low Time Resolution Electron Species Rate	Electrons	64	Count	Spectra Rate	Spectra Flux	PAD, μ	
High Energy Resolution Low Time Resolution Ion Species Rate	Ions	64	Count	Spectra Rate	Spectra Flux	PAD, μ	PSD, Pressure
High Energy Resolution Low Time Resolution TOF $\times$ PH Proton Rate	Protons	32	Count	Spectra Rate	Spectra Flux	PAD, μ	PSD, Pressure
TOF $\times$ E Proton Rate	Protons	14	Count	Spectra Rate	Spectra Flux	PAD, μ	PSD, Pressure
TOF $\times$ E non Proton Rate	Heavy Ions	28	Count	Spectra Rate	Spectra Flux	PAD, μ	PSD, Pressure
Low Resolution High Time Resolution TOF $\times$ PH Proton Rate	Protons	10	Count	Spectra Rate	Spectra Flux	PAD, μ	PSD, Pressure
TOF $\times$ E Ion Species	Ions	64	Count	Spectra Rate	Spectra Flux	PAD, μ	PSD, Pressure
Space Weather Rates	All	NA	Count	Rate	Flux		
Ion Basic Rate	Ions	NA	Count				
Ion Species Basic Rate	Ions	NA	Count				
Electron Basic Rate	Electrons	NA	Count				
Ion Energy Diagnostic Rate	Ions	NA	Count				
Ion Species Diagnostic Rate	Ions	NA	Count				
Priority Events	NA	NA	Event	Event			
Raw Ion Species Events	NA	NA	Event	Event			
Raw Electron Energy Events	NA	NA	Event	Event			
Raw Ion Energy Events	NA	NA	Event	Event			
Auxilary Data	NA	NA	Aux				
Critical Housekeeping Data	NA	NA	HSK				
Magnetic Field and Pitch Angle Data (included as fields in other products)						Pitch Angles	
Spacecraft Coordinates (included as fields in other products)					L, SM	L, GEO, GSM, SM	Others as applicable

Table 7 Higher level data products from RBSPICE

Product	Short Product Name	Duration of Measurement
Electron Energy Basic Rates	EBR	Every S Sectors, if enabled
Ion Energy Basic Rates	IEBR	Every S Sectors, if enabled
Ion Energy Diagnostic Rates	IEDR	Every S Sectors, if enabled
Ion Species Basic Rates	ISBR	Every S Sectors, if enabled
Ion Species Diagnostic Rates	ISDR	Every S Sectors, if enabled
Low Energy Res High Time Res—Electron Spectra	LERHTR-ES	Every S Sectors, if enabled
High Energy Res Low Time Res—Electron Spectra	HERLTR-ES	Every S*N1*N2 Sectors/Spins, if enabled
High Time Res Low Energy Res—Ion Spectra	HTRLER-IS	Every S*N1*N2 Sectors/Spins, if enabled
High Time Res Low Energy Res—TOF × E Ion Energy Spectra	HTRLER-TOF×E-IS	Every S*N1*N2 Sectors/Spins, if enabled
TOF × E Proton Rates	TOF×E-P	Every S Sectors, if enabled
TOF × E Non Proton Rates	TOF×E-nP	Every S*N1 Sectors, if enabled
Low Res High Time Res—TOF × PH Proton Rates	LEHTR-TOF×PH-P	Every S Sectors, if enabled
High Res Low Time Res—TOF × PH Proton Rates	HRLTR-TOF×PH-P	Every S*N1*N2 Sectors/Spins, if enabled
Space Weather Data	SWD	Every Spin—if enabled
Raw Electron Energy Event Data	EEE	Every S Sectors, if enabled
Raw Ion Species Event Data	ISE	Every S Sectors, if enabled
Priority Events Data	Priority	Every S Sectors, if enabled
ERM Data	ERM	Every 180 seconds, if powered

7.2 R_{In} vs R_{Out} Calculations

In general, RBSPICE counts particle events seen by the TOF and SSD systems. The ability of the instrument to count each event is limited by the electronics of the system, causing a failure in counting when counting rates reach approximately 40,000 events per second for the TOF system and 60,000 events per second for the SSD energy mode. When these limits are exceeded, the resulting spectra require scaling to properly represent actual incident event intensities. Scaling is done in four stages.

(1) The TOF system can be commanded to accept a decimation factor of anywhere from each incident event counted to as large as one event counted for every 64 incident events in steps of (incident: count) 1:1, 2:1, 4:1, 8:1, 16:1, 32:1, and 64:1. This factor is adjustable, by command. When the expected incident rates are higher than the TOF system can handle, the decimation factor will be changed, accordingly.

(2) The second scaling stage is modification of the basic counting rates, using the telemetry from the electron (APID: 0 × 312) and ion (APID: 0 × 313) energy basic rates and the ion species (APID: 0 × 315) basic rates. Scaling is done for the start and stop anode rates, as well as for the observed SSD rates, using the following equations:

$$Start_{rate} = \frac{Start0/(Max_{IDLE} * Clk_{period})}{1 - (Start0 * ST_{dead}/Max_{IDLE}) - (Rdt * Rdt_{veto}/Max_{IDLE})} \quad (1)$$

$$Stop_{rate} = \frac{stop0/(Max_{IDLE} * Clk_{period})}{1 - (stop0 * SP_{dead}/Max_{IDLE}) - (R_{dt} * R_{dtveto}/Max_{IDLE})} \quad (2)$$

$$SSDn_{rate} = \frac{SSDn}{(Max_{IDLE} - SSDn_{dt}) * Clk_{period}} \quad (3)$$

where the values of $start0$, $stop0$, $SSDn_{dt}$, SSD, and R_{dt} are taken from the basic counting rate telemetry (either 0×312, 0×313, or 0×315). The other values (except for Max_{IDLE}) are constants of the FPG processor and the value of Max_{IDLE} is derived from the total amount of time allotted for the particular mode of the observation to accumulate counts.

(3) The third scaling stage is a modification of the Energy Mode spectra counts into rates. This stage integrates values from the second stage into the calculation of the rates to adjust the counts due to the inability of the system to identify all incident events. The energy spectrum is a two dimension measurement taken over each of the look directions, i, and for each of the energy bins, j, associated with the particular measurement. This specifically applies to APID's 0×317, 0×318, and 0×319. The equations describing this adjustment are as follows:

$$R_{ij} = \frac{h_{ij}}{Valid_{proc}} * \frac{Valid_{energy}}{IDLE} * C^i_{PKD_{reset}} * C^i_{PUR_{veto}} \quad (4)$$

$$C^i_{PKD_{reset}} = e^{(SSDn_{rate} * PDK_{reset} * Clk_{period})} \quad (5)$$

$$C^i_{PUR_{veto}} = e^{(\frac{SSD_i * PUR_{Veto}}{Max_{IDLE}})} \quad (6)$$

The values of $Valid_{proc}$, $Valid_{energy}$, and $IDLE$ are taken from the basic rate telemetry (either APID 0×312 or 0×313) and used to adjust the counted rate to a more accurate measure of the incident rate.

(4) The final stage of correction is for the Ion Species mode measurements. Again the counts are accumulated in a two dimension array of look directions, i, and "energy bin", j, which is actually the TOF $\times$ E and TOF $\times$ PH ID generated by the event processor for each incident event. The equation describing the modification to the counts is:

$$R_{ij} = \frac{h_{ij}}{Valid_{proc}} * \frac{Valid_{TOF \times E}}{IDLE} * C^i_{PKD_{reset}} * C^i_{PUR_{veto}} * e^{(\frac{Stop0 * SP_{veto}}{Max_{IDLE}})} \quad (7)$$

These equations have been tested using a limited set of laboratory measurements. Random pulsers were used to stimulate the Start and Stop Anodes as well as a single SSD of an Engineering Model. The uncorrelated (background) rates were 1.0×10^6, 5.6×10^5 and 1.0×10^3/sec on the Start, Stop and SSD. Additional random coincident Start, Stop and SSD (foreground) pulses were superimposed on the "background." The foreground pulses were generated with a fixed TOF position on anode and SSD energy. The foreground rates were varied from 1.0×10^3/sec to 7.5×10^6/sec.

The conversion and correction of Start Anode counts (Eq. (1)) and SSD counts (Eq. (3)) for varying input rates are shown in Figs. 29 and 30 with markers indicating the location of the instrument's required and goal rates.

Because a mono-energetic pulse was used to excite only one SSD, the lab data cannot test the formula for correcting the bins of the spectra. Nevertheless, a reduced form of Eq. (7) can be applied, in which the first factor is omitted, to correct the measured Valid event rate. That correction is shown in Fig. 31 for TOF $\times$ E events.

Because the Start Anode pulses start the Event state machine, one sees that in this data set, in which there is a large (>1E6/sec) Start Anode rate, the raw valid rate saturates at a

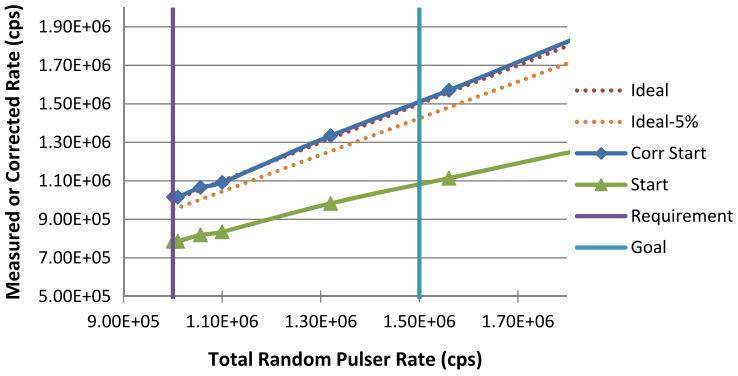

Fig. 29 Start Anode singles rates; raw (*green*) and corrected (*blue*)

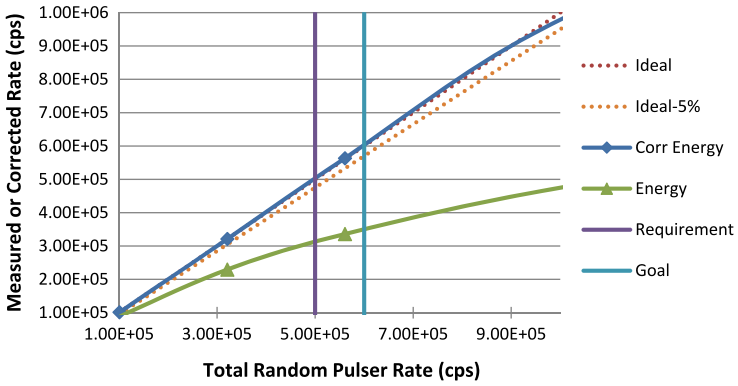

Fig. 30 SSD3 singles rates; raw (*green*) and corrected (*blue*)

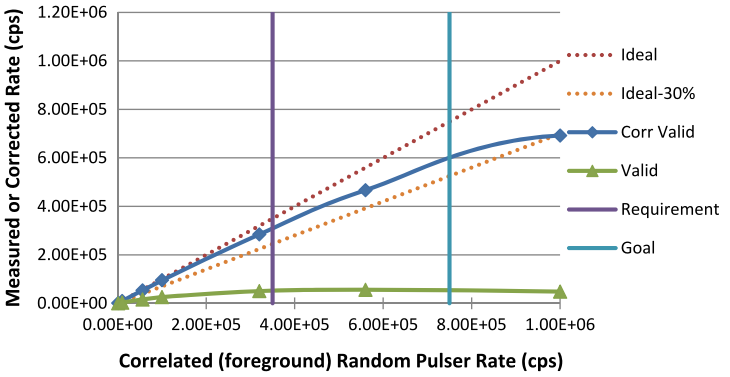

Fig. 31 Valid TOF × *E* rate; raw (*green*) and corrected (*blue*)

somewhat low value due to the state machine deadtime. Nevertheless, after the corrections are made, there is reasonably good tracking of the corrected rate with the foreground input rate.

7.3 Differential Particle Intensity Calculations—Level 2 Data

The conversion of the RBSPICE counting data from rates into differential particle intensities is done in a straightforward method. A calibration file for each of the RBSPICE instruments is used to define the conversion data for each of the data products. The calibration file is an Excel spreadsheet with a worksheet for each of the data products that are to be converted into NASA level 2 data as differential particle intensities. Each worksheet contains a series of entries for each of the energy bins associated with the product. The entries describe the name of the channel, the minimum energy of the bin in units of KeV, the maximum energy of the bin in units of KeV, the mid-point energy of the bin in units of KeV, the geometric factor for the bin if a small pixel is used in units of (cm^2 sr), the geometric factor for the bin if a large pixel is used in units of (cm^2 sr), and finally the efficiency of the channel. Differential particle intensities are then calculated from the derived incident rates (see previous section on R_{In} vs R_{Out} calculations) using the following equation:

$$I = \frac{R}{(\Delta E * G * eff)} \tag{8}$$

with "$\Delta E = E_{\mathrm{High}} - E_{\mathrm{Low}}$" being the channel width.

Which G is used (G_{small} or G_{large}) is determined from the RBSPICE Auxiliary record (APID 0×323) that identifies whether the pixel used is large or small.

7.4 Detailed Discussion of Data Flow

The RBSPICE data processing is done in a series of steps each dependent upon the other with few exceptions.

(1) The most recent data for each of the two spacecraft is downloaded from the Mission Operations Center (MOC) data sites. This process includes a built-in three day delay to allow all of the RBSPICE telemetry to be collected and processed by the MOC. This step also involves downloading all of the Van Allen Probes mission related ephemerids and SPICE kernels that are required for RBSPICE data processing. One aspect of this process is that the SPICE SCLK kernel describing the relationship between Mission Elapsed Time (MET) and Ephemeris Time (ET) is not only downloaded but verified against a MOC-provided time testing web service. If this validation fails, then RBSPICE data processing is stopped until the problem is resolved. This particular time check is a mission requirement that provides a simple means to ensure all of the SOC's data is using the most recent and validated SCLK kernel, thereby ensuring that time stamps on each of the data records are accurately matched from one instrument to another.
(2) A process is executed whereby the downloaded data from the MOC is first moved to a final directory, based upon the APID of the data product. The process then does a full file read to provide a detailed characterization of each file including the actual start and stop times of the included data, the total number of included records, and other relevant information. This information is entered into a processing control database, which is the primary driver for subsequent data processing.
(3) The level 0 (telemetry) data files are then read, and the data is extracted into the database, a Comma Separated Values (CSV) text based data file, and a CDF data file. Not all of the data products are written directly to the database, but instead, only data that must be used by later processing steps (e.g. conversion of counts into rates) is initially stored into the database tables. A prioritization of APID's is done so that Auxiliary and Status data products are read and saved first and then all other data products are processed.

(4) Level 1 processing then continues by converting any data products that include counts into rates. Each of the rate data files is then also written to the file system as both CSV and CDF files. This process also includes a prioritization so that Basic Rate and Diagnostic Rate data products are processed first and then all other files are processed.
(5) Level 2 processing then occurs converting each of the data files from the previous step into particle intensities. Each file written is done as CSV and CDF.
(6) Processing of the magnetic field data is then started. This process includes downloading the most recent magnetic field data from either the EMFISIS or EFW data sites. The files are characterized, and that information is saved in the process control database. The files are then used to generate a look direction data product, which is generated for each of the Level 2 data files at the time cadence of each file. This look direction data product specifies a time stamp, the look direction of each of the RBSPICE telescopes in spacecraft science coordinates, the associated measurement of the magnetic field for the time stamp, and the calculated Pitch Angle of any incident particles measured for each of the RBSPICE telescopes.

This overall processing of the RBSPICE data has been automated so that very little operator intervention should be required. There are a large number of exception—checking steps for each of the processing steps and the processing system is made to compensate for as many of the possible exceptions as possible to allow processing to continue without intervention.

The system has also been built to allow a data operator to follow the processing of each of the data files and verify that the steps of the process succeed. If issues do arise that require intervention, then the system has been built to allow any particular file to be reprocessed at a later time.

7.5 Discussion of Overall Data Organization

The overall RBSPICE data system has been organized to allow a scientist or computer system easy access to any particular data file. The RBSPICE data system is fully described in the document entitled: RBSPICE_SOC_Archive_Dir_Filename_Convention and is available through the RBSPICE SOC web site.

7.6 Discussion of Distribution Protocols Used

The RBSPICE data will be available to the general public through the following web sites: http://rbspicea.ftecs.com and http://rbspiceb.ftecs.com. The data access protocols available are described on each of the web sites, but include data access through standard web ftp protocols for each downloading of each of the data products.

8 RBSPICE Conclusion

The Van Allen Probes Program will provide a transformational view of Earth's space environment, one that has not existed since the discovery of the Van Allen radiation belts more than five decades ago. The comprehensive array of Van Allen Probes instruments with their measurement objectives, combined with the unique two-spacecraft mission, will yield data sets that will provide new understanding of the physics of the radiation belts, including their formation and loss. Importantly, the data sets returned by the Van Allen Probes will be essential for the establishment of new models of the radiation belts and hot plasma environment, models that will be the centerpieces for space program mission design into the future.

The RBSPICE instrument is an essential part of the Van Allen Probes instrument complement. It will provide critical data to answering the three over-arching questions for the Van Allen Probes Program (Sect. 2): that is, RBSPICE will determine "how space weather creates the storm-time ring current around Earth, how that ring current supplies and supports the creation of the radiation belt populations," and how the ring current is involved in radiation belt losses.

Acknowledgements The RBSPICE instrument was supported under a NASA Contract with the New Jersey Institute of Technology, with subcontracts to The Johns Hopkins University Applied Physics Laboratory and to Fundamental Technologies LLC. We thank Heather Mull for her assistance with this paper.

References

S.-I. Akasofu, In memoriam Sydney Chapman. Space Sci. Rev. **11**, 599–606 (1970)

H. Alfvén, A theory of magnetic storms and of the aurorae. K. Sven. Vetenskapakad. Handl., Ser. 3 **18**(3) (1939) (Reprinted in part with comments by Alex Dessler and John Wilcox in Eos **51**, 180–194 (1970))

H. Alfvén, A theory of magnetic storms and of the aurorae, II, The aurorae; III, The magnetic disturbances. K. Sven. Vetenskapakad. Handl., Ser. 3 **18**(9) (1940)

V. Angelopoulos, W. Baumjohann, C.F. Kennel, F.V. Coroniti, M.G. Kivelson, R. Pellat, R.J. Walker, H. Lühr, G. Paschmann, Bursty bulk flows in the inner central plasma sheet. J. Geophys. Res. **97**, 4027 (1992)

S. Barabash, P.C. Brandt, O. Norberg, R. Lundin, E.C. Roelof, C.J. Chase, B.H. Mauk, H. Koskinen, Energetic neutral atom imaging by the Astrid microsatellite. Adv. Space Res. **20**, 1055–1060 (1997). doi:10.1016/S0273-1177(97)00560-7

W. Baumjohann, G. Paschmann, H. Lühr, Characteristics of high-speed ion flows in the plasma sheet. J. Geophys. Res. **95**, 3801 (1990)

P.C. Brandt, S. Ohtani, D.G. Mitchell, M.C. Fok, E.C. Roelof, R. Demajistre, Global ENA observations of the storm main-phase ring current: implications for skewed electric fields in the inner magnetosphere. Geophys. Res. Lett. **29**(20), 1954 (2002). doi:10.1029/2002GL015160

S. Chapman, V.C.A. Ferraro, A new theory of magnetic storms, I, The initial phase. J. Geophys. Res. **36**, 77–97, 171–186 (1931)

S. Chapman, V.C.A. Ferraro, A new theory of magnetic storms, I, The initial phase (continued). J. Geophys. Res. **37**, 147–156, 421–429 (1932)

S. Chapman, V.C.A. Ferraro, A new theory of magnetic storms, II, The main phase. J. Geophys. Res. **38**, 79–96 (1933)

M. Chen, C.-P. Wang, M. Schulz, L.R. Lyons, Solar-wind influence on MLT dependence of plasma sheet conditions and their effects on storm time ring current formation. Geophys. Res. Lett. **34**, L14112 (2007). doi:10.1029/2007GL030189

A.J. Dessler, Swedish iconoclast recognized after many years of rejection and obscurity. Science **170**, 604–606 (1970)

S. Dubyagin, V. Sergeev, S. Apatenkov, V. Angelopoulos, A. Runov, R. Nakamura, W. Baumjohann, J. McFadden, D. Larson, Can flow bursts penetrate into the inner magnetosphere? Geophys. Res. Lett. **38**, L08102 (2011). doi:10.1029/2011GL047016

Y. Ebihara, M. Ejiri, Simulation study on fundamental properties of the storm-time ring current. J. Geophys. Res. **105**, 15843–15859 (2000). doi:10.1029/1999JA900493

Y. Ebihara, M. Ejiri, Numerical simulation of the ring current: review. Space Sci. Rev. **105**(1–2), 377 (2003)

D. Fairfield et al., Geotail observations of substorm onset in the inner magnetotail. J. Geophys. Res. **103**(A1), 103 (1998)

D. Fairfield et al., Earthward flow bursts in the inner magnetotail and their relation to auroral brightenings, AKR intensifications, geosynchronous particle injections and magnetic activity. J. Geophys. Res. **104**(A1), 355 (1999)

M.C. Fok, R.A. Wolf, R.W. Spiro, T.E. Moore, Comprehensive computational model of Earth's ring current. J. Geophys. Res. **106**(A5), 8417–8424 (2001)

C.S. Gillmor, The formation and early evolution of studies of the magnetosphere, in *Discovery of the Magnetosphere*, ed. by C.S. Gillmor, J.R. Sprieter (American Geophysical Union, Washington, 1997)

M.G. Henderson, G.D. Reeves, H.E. Spence, R.B. Sheldon, A.M. Jorgensen, J.B. Blake, J.F. Fennell, First energetic neutral atom images from polar. Geophys. Res. Lett. **24**, 1167–1170 (1997). doi:10.1029/97GL01162

T. Hori, A.T.Y. Lui, S. Ohtani, P.C. Brandt, B.H. Mauk, R.W. McEntire, K. Maezawa, T. Mukai, Y. Kasaba, H. Hayakawa, Storm-time convection electric field in the near-Earth plasma sheet. J. Geophys. Res. **110**, A04213 (2005). doi:10.1029/2004JA010449

V.K. Jordanova, L.M. Kistler, C.J. Farrugia, R.B. Torbert, Effects of inner magnetospheric convection on ring current dynamics: March 10–12, 1998. J. Geophys. Res. **106**(A), 29705 (2001). doi:10.1029/2001JA000047

J.U. Kozyra, M.W. Liemohn, Ring current energy input and decay. Space Sci. Rev. **109**, 105–131 (2003)

J.U. Kozyra, V.K. Jordanova, J.E. Borovsky, M.F. Thomsen, D.J. Knipp, D.S. Evans, D.J. McComas, T.E. Cayton, Effects of a high-density plasma sheet on ring current development during the November 2–6, 1993, magnetic storm. J. Geophys. Res. **103**, 26285 (1998)

L.J. Lanzerotti, A. Hasegawa, C.G. Maclennan, Drift mirror instability in the magnetosphere: particle and field oscillations and electron heating. J. Geophys. Res. **74**(24), 5565–5578 (1969). doi:10.1029/JA074i024p05565

M.W. Liemohn, J.U. Kozyra, V.K. Jordanova, G.V. Khazanov, M.F. Thomsen, T.E. Cayton, Analysis of early phase ring current recovery mechanisms during geomagnetic storms. Geophys. Res. Lett. **26**, 2845 (1999)

G.H. Ludwig, The birth of Explorer I, in *Opening Space Research: Dreams, Technology, and Scientific Discovery* (AGU, Washington, 2011), pp. 245–262. doi:10.1029/2011062SP011

A.T.Y. Lui, R.W. McEntire, S.M. Krimigis, Evolution of the ring current during two geomagnetic storms. J. Geophys. Res. **92**(A7), 7459–7470 (1987)

D.G. Mitchell, K.C. Hsieh, C.C. Curtis, D.C. Hamilton, H.D. Voss, E.C. Roelof, P.C. Brandt, Imaging two geomagnetic storms in energetic neutral atoms. Geophys. Res. Lett. **28**, 1151–1154 (2001). doi:10.1029/2000GL012395

D.G. Mitchell, P.C. Brandt, E.C. Roelof, D.C. Hamilton, K.C. Retterer, S. Mende, Global imaging of O+ from IMAGE/HENA. Space Sci. Rev. **109**, 63–75 (2003). doi:10.1023/B:SPAC.0000007513.55076.00

R. Nakamura, W. Baumjohann, B. Klecker, Y. Bogdanova, A. Balogh, H. Reme, J.M. Bosqued, I. Dandouras, J.A. Sauvaud, K.-H. Glassmeier, L. Kistler, C. Mouikis, T.L. Zhang, H. Eichelberger, A.A. Runov, Motion of the dipolarization front during a flow burst event observed by cluster. Geophys. Res. Lett. **29**(20), 1942 (2002). doi:10.1029/2002GL015763

E.N. Parker, Adventures with the geomagnetic field, in *Discovery of the Magnetosphere*, ed. by C.S. Gillmor, J.R. Sprieter (American Geophysical Union, Washington, 1997)

E.C. Roelof, D.G. Mitchell, D.J. Williams, Energetic neutral atoms ($E \sim 50$ keV) from the ring current—IMP 7/8 and ISEE-1. J. Geophys. Res. **90**, 10991–11008 (1985). doi:10.1029/JA090iA11p10991

A. Runov, V. Angelopoulos, M.I. Sitnov, V.A. Sergeev, M. Bonnell, J.P. McFadden, D. Larson, K.H. Glassmeier, U. Auster, THEMIS observations of an earthward-propagating dipolarization front. Geophys. Res. Lett. **36**, L14106 (2009). doi:10.1029/2009GL038980

A. Runov, V. Angelopoulos, X.-Z. Zhou, X.J. Zhang, S. Li, F. Plaschke, J. Bonnell, A THEMIS multicase study of dipolarization fronts in the magnetotail plasma sheet. J. Geophys. Res. **116**(A5) (2011). doi:10.1029/2010JA016316

A. Schmidt, Das erdmagnetische Aussenfeld. Z. Geophys. **1**, 3–13 (1924)

K. Shiokawa, W. Baumjohann, G. Haerendel, Braking of high-speed flows in the near-Earth tail. Geophys. Res. Lett. **24**(1), 1179 (1997). doi:10.1029/97GL01062

K. Shiokawa, W. Baumjohann, G. Haerendel, G. Paschmann, J.F. Fennell, E. Friis-Christensen, H. Luhr et al., High-speed ion flow, substorm current wedge, and multiple Pi 2 pulsations. J. Geophys. Res. **103**(A), 4491 (1998). doi:10.1029/97JA01680

S.F. Singer, A new model of magnetic storms and aurorae. Eos **38**, 175–190 (1957)

M.I. Sitnov, N.A. Tsyganenko, A.Y. Ukhorskiy, P.C. Brandt, Dynamical data-based modeling of the storm-time geomagnetic field with enhanced spatial resolution. J. Geophys. Res. **113**, A07218 (2008). doi:10.1029/2007JA013003

D.P. Stern, A brief history of magnetospheric physics before the spaceflight era. Rev. Geophys. **27**(1), 103 (1989). doi:10.1029/RG027i001p00103

C. Stoermer, Sur la situation de la zone de fréquence maximum des aurores boréales d'aprés la théorie corpusculaire. C. R. Acad. Sci. **151**, 736–739 (1910)

C. Stoermer, Sur les trajectories des corpuscules electrises dans l'espace sous l'actions des magnetisme terrestre avec application aux auarores boréales, seconde memoire. Arch. Sci. Phys. Nat., Ser. 4 **32**, 117–123, 190–219, 277–314, 415–436, 505–509 (1911)

C. Stoermer, Sur les trajectories des corpuscules electrises dans l'espace sous l'actions des magnetisme terrestre avec application aux auarores boréales, seconde mernoire (continued). Arch. Sci. Phys. Nat., Ser. 4 **33**, 51–69, 113–150 (1912)

R.M. Thorne, Radiation belt dynamics: the importance of wave-particle interactions. Geophys. Res. Lett. **37**(22), L22107 (2010). doi:10.1029/2010GL044990

D.L. Turner, Y. Shprits, M. Hartinger, V. Angelopoulos, Explaining sudden losses of outer radiation belt electrons during geomagnetic storms. Nat. Phys. (2012). doi:10.1038/NPHYS2185

A.Y. Ukhorskiy, B.J. Anderson, P.C. Brandt, N.A. Tsyganenko, Storm-time evolution of the outer radiation belt: transport and losses. J. Geophys. Res. **111**, A11S03 (2006). doi:10.1029/2006JA011690

A.Y. Ukhorskiy, M.I. Sitnov, K. Takahashi, B.J. Anderson, Radial transport of radiation belt electrons due to stormtime Pc5 waves. Ann. Geophys. **27**(5), 2173 (2009). doi:10.5194/angeo-27-2173-2009

R.A. Wolf, J.W. Freeman, B.A. Hausman, R.W. Spiro, R.V. Hilmer, R.L. Lambour, Modeling convection effects in magnetic storms, in *Magnetic Storms*, ed. by B.T. Tsurutani, W.D. Gonzalez, Y. Kamide, J.K. Arballo. Geophysical Monograph Series, vol. 98 (1997), p. 161